JOURNAL OF SPACECRAFT AND ROCKETS
Vol. 50, No. 1, January–February 2013

Hypersonic Shock Wave Impingement on Turbulent Boundary Layers: Computational Analysis and Uncertainty

James L. Brown*
NASA Ames Research Center, Moffett Field, California 94035

DOI: 10.2514/1.A32259

Current status of computational uncertainty for impinging hypersonic shock wave turbulent boundary-layer interactions (SWTBLIs) is evaluated by comparison of computational results with vetted experiments. Employed is one of NASA's production real gas Reynolds-averaged Navier–Stokes finite volume codes, DPLR, along with several commonly used turbulence models. Uncertainty and residual errors, inherent to the analysis and turbulence model implementation, are numerically evaluated for physics quantities of interest. These uncertainty results should prove of value to computational practitioners and developers and to designers making use of modern computational methods to innovate and develop hypersonic hardware such as prototype scramjet engines. Reported are statistical means, variances, and confidence limits of uncertainty measures for the physics quantities of interest to reveal the certitude with which computations of impinging hypersonic SWTBLIs can be relied. A hybrid computational fluid dynamics correlation approach yields improved peak heating estimates in the vicinity of SWTBLIs.

I. Introduction

THE development of hypersonic scramjet concepts relies on accurate flow computations about forebody and engine inlet regions of proposed designs [1]. The unknowns and inexactness of turbulence models, especially in regions of shock wave turbulent boundary-layer interactions (SWTBLIs), are primary limiting factors in such computations and need to be improved. A solid foundation for improvements in simulations of SWTBLIs is best based on understanding the source and level of uncertainties and of residual errors in current capability to compute existing SWTBLI experiments vetted for accuracy and relevance to the hypersonic scramjet mission. To that end, NASA's Fundamental Aeronautics Program has tasked its Hypersonics Uncertainty working group [2] to address hypersonic two-dimensional (2D) and axisymmetric compression corner [3] and impinging shock cases. The purpose of the present paper, then, is to compute selected hypersonic impinging SWTBLI experiments with DPLR [4], one of NASA's production real gas Navier–Stokes codes, and with well-known shear stress transport (SST) [5], K-ω [6,7], and Spalart–Allmaras [8] turbulence models. For the Spalart–Allmaras model, the compressibility modifications of Catris and Aupoix [9] are incorporated, whereas for the SST and K-ω models, the free shear layer compressibility corrections of Sarkar et al. [10], of Zeman [11] and of Wilcox (all as described in Wilcox [7]) as modified by Brown [12] are evaluated for use with hypersonic boundary layers. We then evaluate the uncertainties and sources of error in these computations relative to these selected experiments, reporting the current best practices and uncertainty levels in performing these computations. Such information should prove useful to the scramjet engine designer, also in pursuing improvements in predictive capability, and in providing guidance in design of future experiments.

II. Background

In this section, we discuss the topology of impinging hypersonic SWTBLIs to identify physics features of interest. We then identify correlations used in vetting experiments and for checking consistency in the computations. Uncertainty nomenclature is described and measures of uncertainty used for this study are defined. Next described is the Reynolds-averaged Navier–Stokes (RANS) computational approach including the turbulence models and variations thereof. Finally, we describe the process by which the experiments simulated were selected and provide an overview of those selected experiments.

A. Impinging Shock Wave/Boundary-Layer Topology

The flow topology associated with a generic 2D impinging SWTBLI experiment is depicted in Fig. 1. A zero pressure gradient boundary layer develops on the 2D flat plate test surface. A weak oblique leading-edge shock may either pass above the shock generator, or impact on the shock generator. A shock generator, inclined at angle α, generates the impinging shock at angle Θ from its leading edge. The shock angle Θ may be found by inviscid relations [13] depending on the turning angle α, the rate of growth of the boundary layer on the generator, the Mach number and gas properties. This oblique impinging shock reduces the freestream Mach number from M_1 to M_2, with a loss in total pressure from Pt_1 to Pt_2. The impinging shock will intersect the incoming boundary layer on the test surface at a location roughly $(\mathrm{Zg} - \delta_0)/\tan\Theta$, where Zg is the height of the shock generator leading edge above the flat plate, δ_0 is the boundary-layer thickness at the impingement location, and Θ is the angle of the generated impinging shock. A reflected shock emanates from within the boundary layer in the vicinity of impingement. The shock generator is of finite length, L_g. At the tail end of the shock generator, an expansion fan occurs that weakens the reflected shock downstream of the impingement point. The overall increase in wall pressure in the vicinity of the impingement location is the consequence of a two-oblique-shock inviscid problem accounting for both the impinging and reflected shocks. As the innermost portion of the boundary layer is subsonic, a portion of this shock generated pressure increase propagates upstream of the impingement point. For a shock of sufficient strength, a lambda shock/separation bubble structure forms upstream of the impingement due to the upstream influence of the overall pressure rise. As streamlines just above the separation bubble turn back toward the flat plate to close the separation bubble at the reattachment position, an expansion wave above the separation bubble also forms. Should separation occur, the lambda shock angle is dictated by the property of the oncoming turbulent boundary layer's ability to resist separation due to a given pressure rise. As a consequence, the wall pressure behavior in the vicinity of a shock separated bubble is more a property of the boundary layer than the nature of the particular shock

Presented as Paper 2011-3143 at the 42nd AIAA Thermophysics Conference, Honolulu, HI, 27–30 June 2011; received 20 October 2011; revision received 2 May 2012; accepted for publication 13 May 2012.

*Research Scientist, Aerothermodynamics Branch, MS 230-2. Member AIAA.

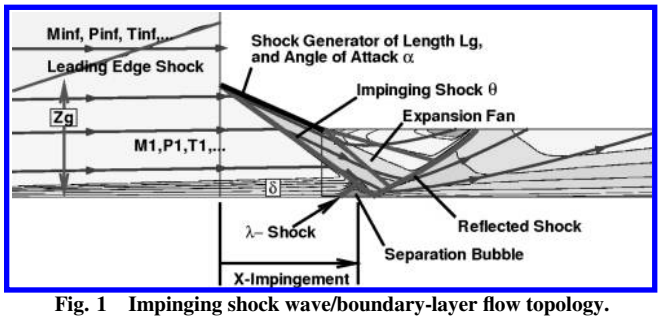

Fig. 1 Impinging shock wave/boundary-layer flow topology.

causing the separation, leading to the free interaction concept derived by Chapman et al. [14], and expanded on by Erdos and Pallone [15], and others [16].

Not obvious from this flow topology description is that the separation λ-shock is unsteady, having time scales comparable to the boundary layer itself (see the ensemble-averaged SWTBLI measurements reported by Kussoy et al. [17] and related discussion by Brown et al. [18]). Shock unsteadiness undoubtedly is one source of uncertainty implicit to RANS methods with current turbulence models.

B. Oblique Shock Relations and Turbulent Correlations

1. *Oblique Shock Relations*

Oblique shock impingement involves two oblique shocks, the first being the impingement shock to align the flow with the shock generator, the second being the reflection shock to realign the flow with the test surface. For a test surface initially aligned with the free stream, two turnings of shock generator angle occur, and for each there is a decrease in Mach number, increase in pressure, density, temperature and entropy, with associated loss of total pressure. The noniterative or direct procedure suggested by Thompson [19], also Wolf [20], is used in determination of this inviscid pressure level as an approximate check on the consistency of the experimental data and computations. This direct form is also used to evaluate total pressure errors for the inviscid problem, and for comparisons of peak pressure for the Schulein experiment.

2. *Turbulent Skin Friction Correlations*

Turbulent skin friction and heating correlations for an undisturbed hypersonic boundary layer are used later to check on the accuracy of the experimental data and computations ahead of the interactions region. Hopkins and Inouye [21] concluded, in comparing with extensive data sets, that the Van Driest II transformation [22,23] of the incompressible adiabatic Kármán–Schoenherr correlation [24] yields compressible skin friction for the zero pressure gradient boundary layer with or without heat transfer to within ≈10% for $T_w/T_{aw} > 0.3$. For cold wall compressible boundary layers with $T_w/T_{aw} < 0.3$ the Van Driest II formulation overpredicts skin friction by as much as 20%. For heat transfer, a Reynolds analogy factor, $Ra_F \equiv 2C_h/C_f$, near unity is used (Coakley [25] gives ≈1.17 ± 15%). This correlation in its compressible form becomes

$$1/(C_f F_c) = 17.08\log_{10}^2(Re_\theta F_\theta) + 25.11\log_{10}(Re_\theta F_\theta) + 6.012 \tag{1}$$

A second form for flat plate skin friction is the Van Driest II transformed correlation of White [26]:

$$(C_f F_c) = 0.455/\ln^2(0.06 Re_x F_x) \tag{2}$$

The Van Driest II compressibility transformation F_c, F_x, and F_θ terms in these correlations are

$$F_c = [(T_{aw}/T_e) - 1]/(\arcsin\alpha + \arcsin\beta)^2 \tag{3}$$

$$F_\theta = \mu_e/\mu_w, \qquad F_x = F_\theta/F_c \tag{4}$$

$$\alpha = (T_{aw} + T_w - 2T_e)/(\Gamma T_e) \tag{5}$$

$$\beta = (T_{aw} - T_w)/(\Gamma T_e) \tag{6}$$

and

$$(\Gamma T_e) = [(T_{aw} + T_w)^2 - 4(T_e T_w)]^{1/2} \tag{7}$$

C_f is the *local* compressible skin friction, Re_θ depends on the local density-weighted momentum thickness, θ, and Re_x depends on local conditions and local distance from the flat plate leading edge. T_{aw} is obtained using a turbulent recovery factor of 0.89. Hypersonic wind-tunnel freestream conditions can approach liquefaction at low temperature (dry air, nitrogen or helium) and the viscosity formulation of Keyes (rather than of Sutherland) should be used in F_c, see Lockman et al. [27].

Turbulent transition is a source of uncertainty for both simulation and experiment, particularly for hypersonics. As transition location is known for the hypersonic experiments considered here, the experimental transition location are used for the simulations. Where transition location is unknown, it may be estimated from correlations based on Re_θ from *laminar* simulations, e.g., Reda et al. [28].

3. *SWTBLI Pressure–Heating Correlations*

A useful correlation of heating variation with pressure for SWTBLIs was found by Back and Cuffel [29], and demonstrated by others, e.g., Holden [30], is that through the attached region of a SWTBLI, but not within a separation bubble if it exists, the pressure and heating scale as

$$Q_{P85} \equiv Q_0 \cdot (P/P_0)^{0.85} \tag{8}$$

This pressure–heating correlation appears valid for a great deal of experimental data regardless of whether the interaction is of the compression corner or impinging shock type. With the difficulty that current RANS methods have in predicting wall heating in the vicinity of shock separated reattachment, it may be more accurate to use the pressure rise past reattachment from the computational fluid dynamics (CFD) simulations and then apply this $Q \approx P^{0.85}$ correlation to arrive at attached SWTBLI heating estimates.

C. Uncertainty

1. *Uncertainty Nomenclature and Definitions*

As the purpose of the current paper is to assess the *uncertainty* and *error* of present-day RANS-based analysis of hypersonic SWTBLIs, a brief review of these and related terms seems called for to ensure consistency with AIAA guidelines and definitions [31]. Also, see Coleman and Stern [32], Roache [33], and Oberkampf et al. [34–36] and Roy and Oberkampf [37]. Definitions taken from [31] are the following:

Verification: the process of determining that a model implementation *accurately represents* the developer's *conceptual description of the model* and the solution to the model.

Validation: the process of determining the degree to which a model is an *accurate representation of the real world* from the perspective of the intended uses of the model.

Uncertainty: a potential deficiency in any phase or activity of the modeling process that *is due* to *lack of knowledge*.

Error: a recognizable deficiency in any phase or activity of the modeling process that *is not due* to *lack of knowledge*.

It is not this paper's purpose to conduct *verification* and *validation* of research-grade computational capabilities. Rather, we use a NASA production code, modified to better examine uncertainties and errors, along with accepted design-grade grids, to identify and quantify those uncertainties and errors present in current design-practice analysis for hypersonic impinging SWTBLIs.

Computational results and experimental measurements, and so derived variables, will be inexact and exhibit statistical behavior related to deficiencies in accuracy of modeling or measuring. *Uncertainty* and *error* are broad categories normally associated with this loss of accuracy. Although similar in that both lead to loss of

accuracy, they differ, in that errors are knowable and correctable (e.g., numerically deficient in model constants), whereas uncertainty is due to a genuine lack of knowledge (e.g., conceptually deficient in form of the physics model).

Uncertainties include the current unknown proper formulation of turbulence models applicable to hypersonic SWTBLI, incomplete reporting by the experimentor of geometry or flow conditions, unknown location of transition, etc. Errors include improper selection of models for the particular case, including but not limited to selection of a turbulence model known inadequate in handling separation, inadequate turbulence model compressible corrections, low numerical order, flux selection, inadequate grid resolution, etc. Errors tend to be correctable, but perhaps tolerated for reasons of practicality. To avoid error in application of a turbulence model, included are details of turbulence model implementation such as expression of turbulent production, compressibility corrections, wall boundary conditions, and adherence to established correlations applicable to the boundary layer and shock wave interaction. As a consequence, in later sections, we examine the sensitivity of several of our turbulent solutions to turbulence model implementation choices. An example of acceptable error, is the use of a coarse grid for preliminary simulations.

As our intent is to establish a benchmark for future reference, we require the algorithm for our uncertainty measures to be unambiguously defined with ease of evaluation. Statistical measures, such as mean, variance and confidence intervals, have clear definition and pragmatic meaning and provide solid basis for the uncertainty measures as developed in the next subsection.

2. *Uncertainty Measures*

A CFD practitioner may ask, "How accurate are my simulations?" Whereas a CFD-user/designer might ask, "What margins do I apply to CFD results for my design?" These pragmatic questions address relevant physics concerns, such as heating, or pressure levels and separation extent. To answer such questions, we construct uncertainty measures based on statistical concepts that account for SWTBLI features of primary interest to the CFD practitioner and the CFD-user/designer.

A natural approach to assessing CFD methods is to examine the discrepancy between simulations of chosen experiments and direct measurements of these same experiments. As a consequence, a new "discrepancy parameter," of form $\mathcal{D} \equiv \sum(\chi_{\text{CFD}} - \chi_{\text{Expt}})/n$, is created as the difference of two corresponding variables drawn from two statistical populations. This new variable, constructed to "compare two quantities or populations," conforms to a well-known statistical problem [38] where examined is whether the first variable is an unbiased estimator of the second variable. This new variable has, in general, a nonzero mean or bias as well as variance that depend on statistical properties of the original variables. For such a discrepancy parameter, statistical quantities such as the 95% confidence interval are found by established procedures [38,39], assuming sample size is sufficient. The bias, variance, and confidence interval of the discrepancy parameter include effects of uncertainty and error from both the computation and experiment. The discrepancy variable, however, does have as a lower bound for its variance and confidence interval magnitude, the variance and confidence interval magnitude of the experimental measurements. Thus, to evaluate CFD by comparison with experiment, the best available experiments must be chosen along with an evaluation for experimental measurement bias and variance.

We first tabulate, for several physics quantities of interest, the discrepancy between experiment and the CFD simulation of that experiment. Then, for a collection of experiments of the same class (e.g., attached or fully separated hypersonic impinging SWTBLI), and for the similar physical effect (such as separation extent, or peak pressure), we combine these tabulated values for each physical effect and each experiment to arrive at measures of uncertainty in terms of confidence interval for the cumulative discrepancy parameter.

The present work uses vetted experiments of the same general type or statistical class, each of which develops a 2D or axisymmetric upstream hypersonic turbulent boundary layer with known properties, and then subjects that boundary layer to a 2D or axisymmetric impinging shock. The experimental design is such that the shock strength may or may not be sufficient to cause the boundary layer to separate, then reattach. Of interest to both the CFD practitioner and the designer making use of CFD arts are relevant physics effects that include 1) the wall heat transfer for the boundary layer just upstream of the interaction; 2) the separation extent, L_s, relative to upstream boundary-layer thickness, δ_0; 3) the separation bubble wall pressure, P_b, relative to upstream mean wall pressure; 4) the separation bubble wall heat transfer, Q_b, relative to upstream wall heat transfer; 5) the peak postimpingement wall pressure, P_p, relative to upstream mean wall pressure; and 6) the peak postimpingement wall heat transfer, Q_p, relative to upstream wall heat transfer.

For each SWTBLI physics effect listed, and for each experimental case simulation, we numerically evaluate a corresponding Δ parameter:

$$\Delta_{Q_0} \equiv (Q_{0,\text{CFD}} - Q_{0,\text{Expt}})/Q_{0,\text{Expt}},$$
upstream boundary layer discrepancy (9)

$$\Delta_{L_s} \equiv (L_{s,\text{CFD}} - L_{s,\text{Expt}})/L_{s,\text{Expt}},$$
separation extent discrepancy (10)

$$\Delta_{P_b} \equiv (P_{b,\text{CFD}} - P_{b,\text{Expt}})/P_{0,\text{Expt}},$$
separation bubble pressure discrepancy (11)

$$\Delta_{Q_b} \equiv (Q_{b,\text{CFD}} - Q_{b,\text{Expt}})/Q_{0,\text{Expt}},$$
separation bubble heat transfer discrepancy (12)

$$\Delta_{P_p} \equiv (P_p/P_0)_{\text{CFD}} - (P_p/P_0)_{\text{Expt}})/(P_p/P_0)_{\text{Expt}},$$
peak pressure discrepancy (13)

$$\Delta_{Q_p} \equiv (Q_p/Q_0)_{\text{CFD}} - (Q_p/Q_0)_{\text{Expt}})/(Q_p/Q_0)_{\text{Expt}}$$
peak heating discrepancy (14)

Those terms involving separation are included only if simulation or experiment indicate separation.

Each Δ parameter corresponds to a single physical effect to be evaluated for each turbulence model simulation for each experimental case and then accumulated in a Table specific to each case examined. We then combine these, for each physical effect, and for each class of SWTBLI, using standard statistical procedures to form a single physics effect, multiexperiment uncertainty "discrepancy parameter" having a sample mean and variance (where the subscript, p, refers to the particular physics effect, $Q_0, L_s, \ldots, Q_p$):

$$\hat{\mathcal{D}}_p \equiv \left(\sum_{1,n_{\text{Expt}}} \Delta_{p,i}\right)/n_{\text{Expt}} \tag{15}$$

$$\mathcal{D}'^2_p \equiv \left(\sum_{1,n_{\text{Expt}}} \Delta^2_{p,i}\right)/(n_{\text{Expt}} - 1) \tag{16}$$

The sum is over all cases that include the physics effect listed previously. Such measures can be evaluated for each listed physics effect, $\mathcal{D}_{Q0}, \mathcal{D}_{L\text{Sep}}, \ldots, \mathcal{D}_{Qp}$. Confidence limits, which include both bias and variance effects, are evaluated for each of the preceding by conventional statistical approaches [38,39].

Measures developed in this subsection contain both error and uncertainty contributions. Such effects are difficult to separate. But, as residual error is anticipated low compared to modeling uncertainties, it is realistic to interpret these "discrepancy" parameters as primarily measures of uncertainty for CFD simulations of SWTBLI. Uncertainty measures constructed in this section for each physical quantity of interest should help a CFD based designer to specify design margins to be applied to simulations or to help a CFD practitioner to focus on aspects of the flow physics simulation most in need of improvement.

D. Computational Methods and Physics Models

1. DPLR RANS

The DPLR (Data-Parallel Line Relaxation) code, one of NASA's hypersonic aerothermodynamics production codes, provides the computations in the present paper. It is a three-dimensional (3D) implicit finite volume, structured-block real gas Navier–Stokes code, with modified Steger–Warming upwind split flux treatment and higher-order spatial differencing. An extensive nonequilibrium finite-rate atmospheric gas chemistry set is available, including options for single- and multiple-temperatures, various gas-diffusion modeling for mixtures of reacting gases, but also perfect gases of various compositions. Turbulence models options include the Baldwin–Lomax, the SST, the Wilcox K-Omega and the Spalart–Allmaras models. Turbulence transition location can be specified, for partial differential equation (PDE) models, by suppression of turbulent production for those regions determined to be laminar. More detail can be found in the DPLR users manual [40].

2. Turbulence Models

Mathematical modeling of turbulence is perhaps the largest source of uncertainty in RANS simulations. The models in this study include the Baldwin–Lomax algebraic, the Spalart–Allmaras one-equation, and the Menter SST/K-ω and Wilcox-2006 K-ω two-equation models. These eddy viscosity models have a long track record in scientific and industrial applications. However, these models require development to account for experiences peculiar to hypersonics heating applications.

The Baldwin–Lomax model [41] is widely used and published, with little need to repeat here. One adaption is made for hypersonic flows, that of a compressible form for $y^+ \equiv \rho u_{\tau_w} d/\mu_w$ in the Van Driest damping term, where ρ is *local* density, d is closest-wall-normal distance, and all other terms are for the nearest wall location. The model is perhaps the best formulation where hypersonic "acreage heating" is the primary concern, and where the flow remains attached. With specification of transition, turbulent Prandtl ($Pr_t \approx 0.9$) and turbulent Schmidt numbers (for gaseous mixtures, $Sc_t \approx 0.7$), and for smooth wall conditions, RANS simulations using the Baldwin–Lomax model are often within 10% of heat transfer measurements. However, where a strong shock interacts with a turbulent boundary layer and separation is likely, the PDE-based models gain greater acceptance and are of primary interest for this study.

To avoid ambiguity, standard forms of the Spalart–Allmaras, SST and K-ω turbulence models are specified in Appendix A. In the following subsection, implementation of these models into the DPLR code is described, along with variations to be explored.

3. PDE Turbulence Model Implementation, Corrections and Variations

The PDE turbulence models (SST, K-ω, and Spalart–Allmaras), are all implemented on the same subroutine templates. These model implementations use point-Jacobi, with accelerated time advancement and subiterations requiring Jacobians of form $\partial F_{i+1/2}/\partial U_{i\pm1}$, etc. The turbulence spatial differencing is second-order within the cell from the volume integral method of Gauss–Ostrogradsky (divergence theorem), except for first (optionally second) order terms evaluated at cell faces. For Gauss–Ostrogradsky, the cell volume is also so derived. The numerics have proven robust for even the strongest shocks and with flows that approach near vacuum, and turbulent cases often converge faster than related laminar cases.

Some adaptations to these models for hypersonic applications have proven necessary. They are provided within DPLR either as the default implementation or, for this study, as command-line options. The model options include spatial accuracy, time advancement, flux treatments, turbulence production variants, "free-viscous-shear" compressibility correction choices, and wall boundary condition treatments and the compressibility modifications of Catris and Aupoix. Different RANS codes may actually differ in their default SST model implementation choices. This can lead to a variation in simulation results from different RANS codes even where the same nominal model is used on the same grid. The consequence is a loss in confidence in turbulence model results and an increased perception of uncertainty in the turbulence model amongst the CFD community.

The wide range of SST model options implemented in DPLR for this study are described in Appendix B, along with a Mach 10, cold wall flat plate study, emphasizing wall heating sensitivity to these various implementation options. Those results are briefly summarized here because they are used later in the Results section. The DPLR defaults for these turbulence model options are also indicated in Appendix B.

Appendix B study establishes that the majority of the SST model implementation choices examined have only small effect on the flat plate wall heating results relative to the DPLR "standard" form employed. Regrettably, the standard wall boundary condition for the SST model displays considerable sensitivity of wall heating with grid near wall spacing when $y_1^+ > 0.3$. Likewise, the standard form of the free shear compressibility corrections in the SST (and related K-ω) model brings about significant erroneous reduction in computed hypersonic wall heating. In contrast, the form of the turbulent production term, whether of "vorticity" based, or "strain" based have little effect, for the Mach 10 flat plate examined. Further shown in Appendix B study is the Catris and Aupoix viscous diffusion modification (the SST and K-ω version), which is intended to improve log-law compressible boundary-layer behavior, proves unneeded.

A positive finding in Appendix B is that one wall boundary condition option (e.g., WallBC1.6 defined in Appendix B) significantly reduces the y_1^+ grid sensitivity of wall heating otherwise experienced. This improved wall treatment actually blends into the implicit solution procedure the near wall analytical solution for those cells near a solid wall, replacing the need for a conventional wall boundary condition. In a later section, this simple-to-incorporate wall boundary condition option when applied to a separated impinging SWTBLI brings about improved reattachment heating. Unless otherwise stated, however, Navier–Stokes results presented make use of the conventional wall boundary condition.

A second positive finding regarding SST implementation choices is a simple modification to the free shear compressibility corrections eliminates their otherwise negative impact on hypersonic wall heating and thereby facilitates their more general use. When applied to hypersonic impinging SWTBLI separated cases, improvements in the separation extent are found relative to the standard approach of not using free shear compressibility corrections for wall bounded flows. These easily modified free shear compressibility corrections found worthwhile are the modified-Sarkar, modified-Zeman, and modified-Wilcox forms.

E. Experimental Case Selection Process

An early task in this study was to identify the impinging hypersonic SWTBLI experiments to be simulated as the basis for the uncertainty analysis. To entertain evaluation of statistical quantities, we desired a minimum of three such experiments but were hopeful of more. Of particular value in identifying vetted experiments conducted up to the early 1990s was the review and experimental tabulation reported by Settles and Dodson [42,43]. Settles and Dodson were commissioned by NASA to identify and review supersonic and hypersonic experiments of several types, including compression corner, impinging shock and fin generated SWTBL experiments. Further hypersonic impinging SWTBLI experiments, reported subsequent to Settles and Dodson, were searched for based upon the later reviews of Roy and Blottner [44], Delerey and Marvin

[16], Knight et al. [45], as well as extensive search of AIAA and other papers and publications for both experiments and simulations of experiments, recent Ph.D. dissertations and reports from Foreign national agencies, and of Bradshaw's online turbulence bibliography database [46].

Specific factors for the impinging SWTBLI experiments considered for this study were: 1) hypersonic conditions ($M > 5$ preferably high enthalpy *and* real gas); 2) geometry well defined as to test boundary-layer surface relationship to the shock generator; 3) well-defined and (steady) freestream (P_T, T_0) conditions; 4) well-defined upstream 2D cold wall turbulent boundary layer with known transition and in agreement with accepted (e.g., Kármán-Schoenherr [26]) correlations; 5) attached, incipient separation, and fully separated cases, with postreattachment wall heating conforming to $(Q/Q_0) \approx (P/P_0)^{0.85}$ correlation; 6) instrumentation (use of established methodology) [a) redundancy, direct and indirect; b) wall pressure (most reliable); c) wall heating; and d) wall shear stress]; 7) flowfield measurements, with a) pitot and temperature probe surveys, log-law of wall region, and b) flow visualization, surface and flowfield; 8) reliability of other reported experiments at same facility; and 9) previous reported simulations of experiment by other authors.

Of the hypersonic experiments identified, only three were chosen for this study. Regrettably, no turbulent hypersonic experiments with real gas effects were identified, although one laminar experiment was located. As a consequence, real gas effects for hypersonic impinging SWTBLI flows are examined herein by construction of a "nominal-trajectory" flight case sensitivity study.

1. *Schulein Mach 5 Experiment Overview*

Schulein et al. [47,48] conducted this experiment, which proved to be well executed, thoroughly documented, and with excellent instrumentation. It was conducted in the DLR Göttingen Ludwieg Tube facility, having a useful test time of 0.3 s for the test conditions. The nominal test conditions were $P_T = 2.12$ MPa, $T_0 = 410$ K, $T_w = 300$ K, $ReU = 37 \cdot 10^6/\text{m}$, $U_\infty = 830$ mps, and $H_{0,\infty} = 0.41$ MJ/kg, with air as the working medium. The instrumentation included Pressure Systems, Inc., 32-port pressure modules (also used extensively by NASA). Redundant skin friction measurements were obtained by independent approaches: 1) the proven oil-film technique [49–53] and 2) the well-established indirect log-wall deduction of wall skin friction from probe measurements. Wall heating was as determined from measured temperature variation with time and relying on semi-infinite wall assumptions. Confidence in the wall heating measurement can be indirectly deduced from pressure measurements from the $(Q/Q_0) \approx (P/P_0)^{0.85}$ correlation. The experimental uncertainties are determined to be $\approx$2% for pressures, $\approx$10% for skin friction, and $\approx$20% for heat transfer. Probe surveys were obtained, as well as high-quality schlieren flow visualization for all cases. The upstream boundary layer developed on a 2D flat plate of distance $x_0 = 0.350$ m before the interaction, and conformed to proven turbulent correlations. Four flow cases are: 1) G0, a 2D nominal zero pressure gradient flat plate boundary layer; 2) G6, an attached impinging SWTBLI case with 6 deg nominal shock generator angle; 3) G10, an incipient impinging SWTBLI case with 10 deg nominal shock generator angle; and 4) G14, a separated impinging SWTBLI case with 14 deg nominal shock generator angle.

The shock generator is relatively "long" with respect to the boundary-layer thickness, $L_g/\delta_0 \approx 1000$ giving spatial separation for the various topological features of the impinging SWTBLI flowfield.

Further publication in the open literature describes the experiment procedure in depth [48]. Prior computations for this experiment have been reported [54,55] allowing for comparison of the present work with independent simulations.

2. *Murray Mach 8.9 Experiment Overview*

The experiment [56,57] was conducted in the Imperial College nitrogen gun tunnel previously used in the classic hypersonic compression corner studies of Elfstrom [58] and of Coleman and Stollery [59]. It has a steady test time of 5 ms. Hillier, as advisor, oversaw a series of studies [57,60], culminating in the PhD dissertation of Murray. The experimental test surface was a hollow axisymmetric cylinder, of 75 mm diameter. The attached case shock generator is an axisymmetric cowl of 4.7 deg internal angle, whereas the cowl for the fully separated case has a 10 deg internal angle. Instrumentation is limited to wall pressure, wall heating and schlieren flow visualization. Wall heating was deduced based on one-dimensional conduction and the time history from thin-film resistance temperature gauges. Nominal test conditions are $P_T = 60$ MPa, $T_0 = 1150$ K, and $M = 8.9$, giving $U_\infty = 1445$ mps. The unit Reynolds number for these conditions is $ReU = 47.4 \cdot 10^6/\text{m}$. Total enthalpy, $H_{0,\infty} = 1.1$ MJ/Kg, of the experiment, with nitrogen as the working gas, is insufficient for N_2 dissociation and related real gas effects. Data presented in this paper were digitized from Murray's figures using the g3data [61] program.

Wall pressure measurements on the cylinder upstream of shock impingement indicate an axial gradient in Mach number for this facility, making it initially difficult to match, at the nominal test conditions, the wall pressure distribution from simulations with the corresponding upstream boundary-layer measurements. A search led to the report of Mallinson et al. [62], whose measurements on a cylinder indicated a conical flow in the gun tunnel nozzle rather than a uniform free stream. Mallinson et al. then deduced the conical flow angularity variation of the nozzle. An initial profile, corresponding to such a conical flow, was analytically expressed and numerically generated as input for the present simulations so as to reasonably replicate the upstream wall pressure distribution on the cylinder while conforming to the nominal free stream conditions. All simulations conducted in this study for the Murray cases use this approach. The boundary-layer results of Mallinson et al. also indicate transition location that is used for the present simulations. A wall temperature of $T_w = 300$ K is assumed for the simulations.

The shock generator is "short" relative to the upstream boundary-layer thickness at $L_g/\delta_0 \approx 100$, meaning that the shock originating from the shock generator leading edge and the expansion fan from the shock generator trailing edge, merge and thereby mitigate shock impingement effects.

Murray provides experimental error estimates of $\pm$2.3% for pressure measurements, and $+8.7\%$ to -2.2% for heat transfer measurements.

3. *Kussoy and Horstman Mach 8.2 Experiment Overview*

The experiment [63] was conducted on a 2D flat plate in the NASA Ames Research Center "$3 - 1/2$ ft" Hypersonic facility. It was a high-pressure, gas-heated pebble-bed blowdown facility, having long run time.

The nominal test conditions are $P_T = 60$ atm, $T_0 = 1166$ K, giving $H_{0,\infty} = 1.17$ MJ/Kg, and $ReU = 5 \cdot 10^6/\text{m}$. The working gas is air. Tunnel test time is given at 20 s, but the facility had a useful test time of 3 min under these conditions. The flat plate test surface was water-cooled. Wall temperature was $T_w = 300$ K nominal, and the wall temperature rose only 5 K during a 3 min run, with cooling turned off while heat transfer was measured. Variation in total temperature during a 3 min run is given at $\approx$50 K. Run variations in pressure and Mach number were found to be less than 0.5%.

The test surface was a sharp flat plate, 76 cm wide, 220 cm long. The plate is pitched at -2 deg angle of attack to increase the test Reynolds number, and provide a uniform 2D flow over the plate. The shock generator could be inclined at angles from 5–15 deg to determine incipient separation. The location of the shock generator leading edge relative to the leading edge of the flat plate varied so that the shock impinges on the flat plate at the location of densest gauge placement (1 cm spacing), but is given for each case. The primary case herein considered is that of the 10 deg wedge with fully separated flow.

The pressure cells used were a high-accuracy Barocell for P_T and Pressure Systems, Inc., modules similar to that of Schulein. Pressure calibrations of all pressure instruments were traceable to National standards by means of a dead-weight test-stand used extensively in these facilities. The experimentor estimates experimental uncertainty

for surface pressure as being ±10% or ±80 N/m whichever was higher. However, this seems to be an overly conservative estimate based on related facility reports.

Heat transfer rates were measured by two means: a transient thin-skin method; and, a thermopile method. The transient thin-skin method used chromel-constantan thermocouples spot welded to the test bed, and relied on a 10–50 K temperature rise (with cooling disconnected) during a 20 s heat transfer run. The thermopile method made use of Schmidt–Boelter gauges, measuring a temperature difference across a known substrate. Surface heat transfer was corrected, by a simple procedure described, for run variations in total temperature of up to 50 K or about 0.5%. However, overall uncertainty in heat transfer included uncorrected lateral conduction effects and is cited to be ±10%, which seems realistic.

Skin friction and boundary-layer properties were obtained by pitot and static pressure probe surveys. Total temperature probe surveys were also conducted. Skin friction was deduced based upon log-law-of-wall relation with measurements transformed by Van Driest-II relation [23], and is given for the upstream boundary layer as $Cf = 0.00098$, with $\delta_0 = 3.7$ cm, $\delta_0^* = 1.59$ cm, $\theta_0 = 0.094$ cm. Further upstream boundary-layer properties are $\tau_{w,0} = 19.6$ N/m^2, and $Q_0 = 10,400$ W/m^2. Upstream freestream properties are $P_\infty = 430$ N/m^2, $\rho_\infty = 0.0187$ kg/m^2, $T_w = 300$ K, $T_\infty = 81$ K, $U_\infty = 1446$ m/s.

The flow field uncertainties were estimated to be ±2% for the total temperature, ±10% for the static pressure, ±6% for the static temperature, ±12% for the density, ±3% for the velocity, ±3% for yaw angle, and ±5% for the pitot pressure. The uncertainty in Y was ±0.02 cm. No uncertainty estimates for boundary-layer properties are provided by the experimentor, but ±5–10% seems appropriate.

Another uncertainty comes about because the shock generator is moved over a limited range, about ±3%, in X-position between runs, so as to reposition the shock impingement location over the array of fixed pressure taps and fixed heat transfer gauges to improve resolution of these measurements. As the X-dependence in upstream boundary-layer properties is weak, no accounting is made for this positional uncertainty.

4. *"Nominal-Trajectory" High-Enthalpy, Turbulent Cases*

No *turbulent impinging* SWBLI experiments were found reported with high enthalpy sufficient to exhibit real gas effects. However, the *laminar compression corner* SWBLI experiment of Mallinson et al. [62] shows real gas effects. The experiment was conducted over a Mach and total enthalpy range ($M = 9.0$, 7.5, and 7.4, and $H_{0,\infty} = 2.85$, 13.7, and 19.1 MJ/Kg respectively) to examine real gas effects on separation. Total pressure was in the range of $P_T \approx 21.6$–22.6 MPa. An increase in ramp angle varied the interaction strength from attached to fully separated. By examining measured behavior relative to correlations to account for known compression corner dependencies, the influence of *total enthalpy* was deduced. Observed was that a total enthalpy increase brings about partial, if slight, dissociation within the separation bubble, with a decrease in separation extent and a more diffuse rise in reattachment heat transfer.

As a physical basis for the observed *laminar compression corner* real gas effect, a decrease in the gas temperature rise, whether directly due to dissociation within the separation bubble or indirectly due to variable specific heat, brings about a decrease in realized pressure rise, with consequent decrease in separation extent. Therefore, it was decided to initiate a sensitivity study to see if these effects occur for computational simulations of turbulent impinging shock interactions as well.

To perform a real gas "sensitivity" study on *turbulent impinging* SWTBLI cases and to improve "ground-to-flight" traceability, we constructed "nominal-trajectory" high-enthalpy, turbulent cases relevant to scramjet engine performance. The nominal "flight" conditions were derived from the published trajectory of Billig [1] for typical scramjet conditions. Two test case conditions were chosen: one similar to that of Kussoy and Horstman [64] at Mach 7, with $\rho_\infty = 4.401 \cdot 10^{-2}$ Kg/m^3, $T_\infty = 220.94$ K, $H_{0,\infty} = 2.4$ MJ/Kg, $T_w = 500$ K, and the other for a higher altitude Mach 14 case, where $\rho_\infty = 9.811 \cdot 10^{-3}$ Kg/m^3, $T_\infty = 246.93$ K, $H_{0,\infty} = 9.97$, and $T_w = 400$ K. Both Mach numbers had an attached case with shock generator angle of 5.5 deg, and a separated case with shock generator angle of 10 deg. Only the 10 deg shock generator Mach 14 case exhibited real gas effects and is the only one presented. The upstream boundary-layer development length was chosen to ensure turbulent flow, with transition based on a Re_θ correlation derived from the three experiments. Cases were run with air as a perfect gas, with air as a calorically imperfect gas, and with air using the Park five-species chemistry model [65].

III. Results

In this section, we first examine upstream boundary-layer development. Note that we describe in Appendix B, a brief study of sensitivity of a Mach 10, cold wall turbulent boundary layer to implementation details of the SST turbulence model and incorporate those options that had a positive effect into the main body of this work so as to further examine their impact on these cases as well. Then, a grid sensitivity study for an inviscid form of the Schulein shock wave experiment is conducted to document an inviscid error source that must be dealt with to properly conduct these types of simulations. Next, the Schulein SWTBLI experiment will be examined in detail for the attached, incipient separation, and fully separated cases. Subsequently, the Murray SWTBLI cases and the Kussoy SWTLBI cases will be examined. The section is completed by showing the results of the uncertainty analysis.

A. Flat Plate Cases

As the boundary-layer response to the SWTBLI depends on the state of the upstream boundary layer, it is of benefit to briefly examine the upstream boundary-layer development for each of the selected experiments to ensure proper specification of flow conditions and to the computation of the boundary layer immediately upstream of the SWTBLI. Documentation of each experiment precludes concern for significant 3D spanwise effects, and is not further addressed here.

1. *Schulein $M_\infty = 5$, 2D Flat Plate Boundary Layer*

RANS solutions are obtained, for the flat plate boundary layer upstream of the Schulein et al. [47] interaction, using DPLR V4021 in its *standard* form, for the Baldwin–Lomax, Spalart–Allmaras, SST, and Wilcox-2006 K-ω turbulence models. For the SST and K-ω models, the *standard* version of DPLR is equivalent to the choice of vorticity-based production, no compressibility correction, first-order convective terms, and the iWallBC0 = 0, iWallBC1 = 0, iOmegaAn = 2 model implementation options. The grid used for the flat plate solutions is $528 \times 3 \times 128$ in three blocks. Initial cell off the surface is sized so $y_1^+ \approx 0.05$ and ReCell = 0.25. Transition is set, from the experiment, to occur at $x_{\rm tr} \approx 0.1$ m, for which laminar simulations give $Re_\theta \approx 500$.

Figure 2 is a plot of wall shear stress against distance from the flat plate leading edge, showing the experiment results, the Van Driest-II transformed correlation of White, and the RANS simulation results for the several turbulence models. Note that common practice for the Re_X correlation is to employ a virtual origin shift to account for transition. This plot shows excellent consistency of the experimental data with this established correlation. The Spalart–Allmaras model agrees with correlations and experimental data for the wall shear stress, while the remaining models, including the Baldwin–Lomax model, appear ≈10% low. A plot of computed results for wall shear stress versus Re_θ with the Van Driest-II transformed correlation of Kármán–Schoenherr gives similar comparison and is not shown.

In Fig. 3, the Baldwin–Lomax, SST, and K-ω turbulence models agree amongst themselves and the experimental measurements for wall heating within experimental scatter, but the Spalart–Allmaras model overpredicts heating by 10%. This contrasts with the wall shear stress comparison, where the relative performance of the turbulence models is reversed.

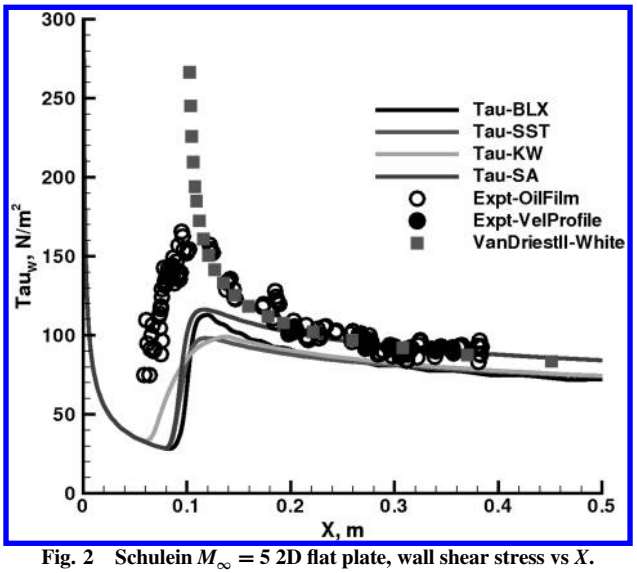

Fig. 2 Schulein $M_\infty = 5$ 2D flat plate, wall shear stress vs X.

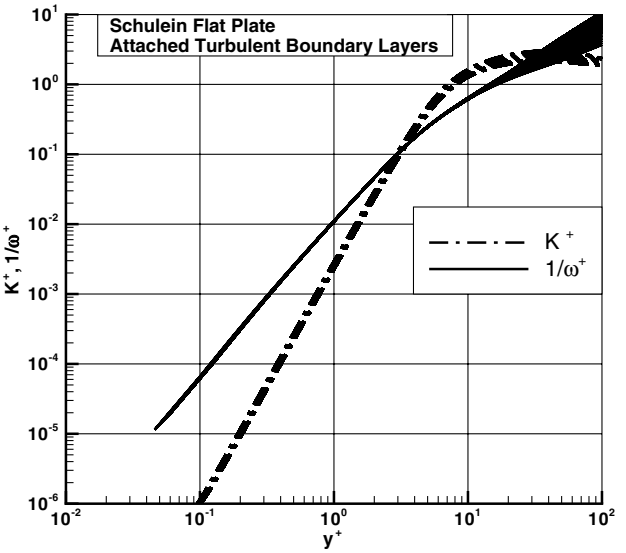

Fig. 4 Schulein $M_\infty = 5$ 2D flat plate, SST model-attached turbulent boundary-layer normalized K-ω profiles. All turbulent profiles are plotted.

Figure 4 shows profiles of normalized turbulence variables, K and ω, for SST solutions for the Schulein flat plate. For the near wall sublayer, sufficient terms in both the K and ω equation become negligible for the PDEs to tend to nonlinear ODEs subject to analytical solution. These solutions are known, e.g., Wilcox [7] with $\omega_{\text{sublayer}} = 6\mu/\beta_\omega \rho y^2$, and $K_{\text{sublayer}} \approx a y^n$, (due to a singularity, the constants a, n require fit specific to the model). Plots of normalized K^+ and $1/\omega^+$ can then be used for *verification* of the turbulence solution procedure for at least the sublayer because these are analytic solutions against which CFD profiles can be compared. Significantly, Fig. 4 shows not merely a single profile, but actually *all* turbulent profiles for this particular case. Other plots, not shown, containing *all* the normalized profiles for locations fully turbulent also agree equally with each other for all cases contained in this paper.

2. *Murray $M_\infty = 8.9$, Axisymmetric Cylinder Boundary Layer*

The test surface is a hollow cylinder of 75 cm diameter with its axis aligned along the nozzle centerline. In our first attempt to compute the Murray cases, we made the simplification of constant freestream conditions at Murray's reported nominal test conditions and found that it was necessary to account for the streamwise pressure gradient of this facility.

Fortunately, the report by Mallinson et al. [66] provides the required calibration details for the Imperial College gun tunnel nozzle that allows one to correct for this gradient. Mallinson describes the facility as having a conical nozzle design that yields a diverging set of streamlines. To account for the pressure gradient caused by the conical diverging streamlines of the tunnel nozzle, the flow angle was calculated from a fit of the curve given by Mallinson, with flowfield divergence angle of $\alpha = 5$ deg/m $\cdot R$, where α is the off-centerline conical divergence angle, and $R = \sqrt{y^2 + z^2}$ is the distance off-centerline at the X-station of the cylinder leading edge. The (u, v, w) components for the computational inlet boundary at the cylinder leading edge were then computed. This CFD setup was used for all Murray results in this current paper.

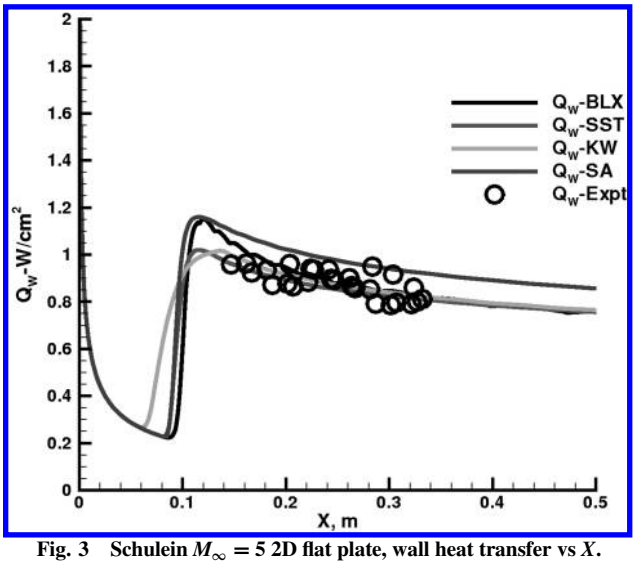

Fig. 3 Schulein $M_\infty = 5$ 2D flat plate, wall heat transfer vs X.

From Mallinson's experiment, transition to turbulence occurs on the test cylinder at 0.09–0.15 m from the cylinder leading edge, start to finish. Re_θ for transition (laminar calculations) is from 750–940.

The computations were based on a 3D grid for this axisymmetric flow of $256 \times 9 \times 256$, with the first point off the wall located at $y^+ = 0.1$. Only the quarter-plane was calculated. Computations for the test cylinder were performed using both the Baldwin–Lomax and the SST two-equation turbulence model, with specified transition location, and with the further two options of a simple uniform freestream at the inlet boundary condition of the cylinder leading edge, or of a pointwise boundary condition at the cylinder leading edge that represents the diverging streamlines as described previously.

Figures 5 and 6 compare the current computations for the cylinder test surface of Murray relative to the data of Mallinson et al., for wall pressure and for wall heating, respectively. The computed wall pressures in Fig. 5 show better agreement with experiment using the pointwise diverging nozzle boundary condition for the inlet boundary face rather than using the simple uniform nominal freestream. The effect of the diverging nozzle flow, of course, is a streamwise drop in cylinder pressure associated with a streamwise increase in boundary-layer edge Mach number. Mallinson also describes comparisons they made of computations for the flow over the cylinder using a nominal uniform freestream with another computation with input conditions *calibrated* so that their final computed results almost precisely agree with the measured cylinder pressures.

With the use of a simple uniform freestream, Mallinson computed 3–5% difference in his calculated cylinder wall pressure and that actually measured, somewhat better than the current computations for uniform freestream, which range from -10% at the cylinder leading edge to $+2\%$ at $X = 0.6$ m. For the current computations with the diverging nozzle boundary condition, there exists improved comparison with calculated wall pressures, but still with differences amounting from -2% at the cylinder leading edge to $+2\%$ at

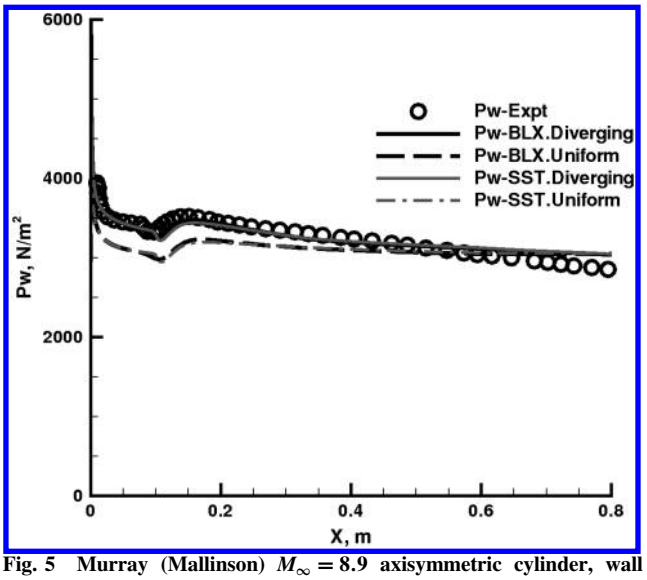

Fig. 5 Murray (Mallinson) $M_\infty = 8.9$ axisymmetric cylinder, wall pressure vs X.

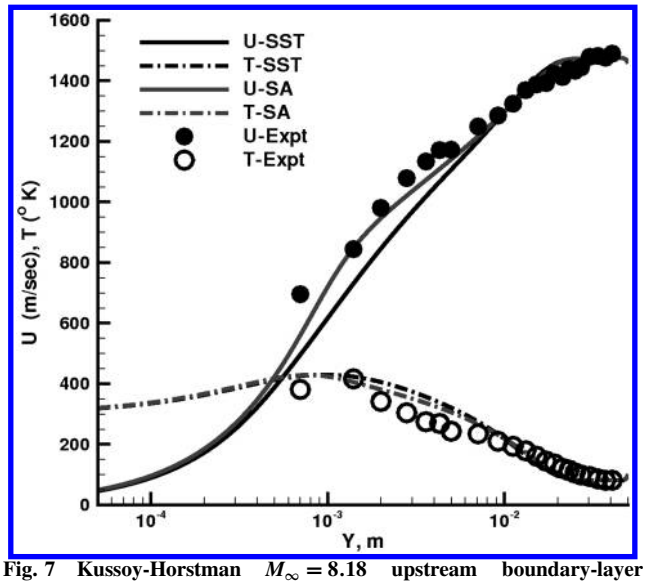

Fig. 7 Kussoy-Horstman $M_\infty = 8.18$ upstream boundary-layer profile.

$X = 0.6$ m. There is little difference in computed pressure due to turbulence model.

Figure 6 shows the wall heating comparisons. The Baldwin–Lomax result using the diverging nozzle boundary condition gives the best agreement with measured heat flux, starting 7% low just after transition, and 4% high at $X = 0.6$ m. In contrast, the SST wall heating result using the diverging nozzle boundary condition starts 11% low just after transition, and becomes 12% high at $X = 0.6$ m.

Based on our lack of knowledge as to initial boundary-layer conditions we estimate a contribution of $\Delta_{Q_0} \approx 10\%$ to the overall computational uncertainty for the Murray cases.

3. Kussoy and Horstmann $M_\infty = 8.2$, 2D Flat Plate Boundary Layer

Kussoy provided measurements for only a single boundary-layer profile just upstream of the SWTBLI, with the intent that simulations match this profile, starting the grid at the upstream measurement location with a specified inlet profile. That is not the approach for this uncertainty study. Rather, we compute the flow over the entire geometry, as a designer would, starting with the flat plate leading edge, and then compare with upstream boundary-layer measurements. These simulations use a four-block grid, having $96 \times 3 \times 128$ cells each, and with $y_1^+ = 0.2$. Transition was not available from the experiment and was set in the CFD simulations at $x_{tr} = 0.4$ m from the leading edge to give Re_θ intermediate to the Schulein and Murray cases.

Figure 7 compares the measured velocity and temperature profiles for the upstream boundary layer with profiles obtained with the Spalart–Allmaras and with the SST turbulence models. There appears reasonable agreement of the CFD results with experiment in the outermost portion of these profiles, where both models appear to be within 5–7%. The Spalart–Allmaras profiles (at 5% in velocity, 15% in temperature) appear to agree better with experiment than does the SST profiles (at 12% in velocity, and 15% in temperature) for the log-law region. The CFD simulations for these models are within 5% of the stated experimental heat transfer for the upstream boundary layer. The documentation for this experiment gives skin friction (at $\tau_w = 19.2$ N/m^2) for this measured profile. The CFD results for wall shear stress are 17.5 N/m^2 or 10% low for the SST model and 18.77 N/m^2 or 5% low for the Spalart–Allmaras model. Based on our examination of the measured profile, the best information describing the upstream boundary layer are the profiles in velocity and temperature themselves and the cited $P_w = 430$ Pa, and $Q_{w,0} = 10.4$ W/cm^2. Using these two metrics, the CFD results describe the initial upstream boundary layer to within ≈10% uncertainty.

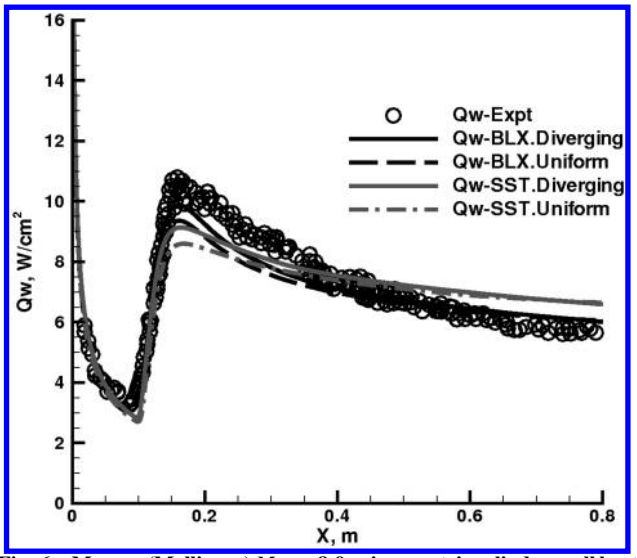

Fig. 6 Murray (Mallinson) $M_\infty = 8.9$ axisymmetric cylinder, wall heat transfer vs X.

B. Inviscid Impinging Shock Case

Although the primary focus for this paper is on the uncertainty in hypersonic SWTBLI CFD simulations due to deficiencies in turbulence modeling, there remains an inviscid-related error source that warrants examination. This present work supports scramjet technology development. The scramjet inlet feeds the combustor with air compressed by a sequence of SWTBLIs, while retaining as high a total pressure as possible. With as many as five to seven interactions total for a scramjet engine inlet, the inviscid prediction of each oblique shock problem must be highly accurate. The magnitude of errors associated with the inviscid part of this problem is estimated by construction of an *inviscid* counterpart to Schulein's 14 deg experimental case. Total pressure is then tracked along selected streamlines, and compared with simple oblique shock relations [13], as supplemented by the direct solution approach [19,20].

Figure 8 shows Mach color contours for DPLR simulations, but run in the *inviscid* mode only. Also in Fig. 8 are streamlines originating at the inlet. The streamline going down the centermost portion of the computational domain is shown as a *bold dash-dot* line. Figures 9–11 are plots showing the total pressure variations along each of these streamlines, for different grid refinements, again with the total pressure results for the centermost streamline shown as a *bold dash-dot* line. Figure 9 is for a coarse grid of $528 \times 3 \times 128$

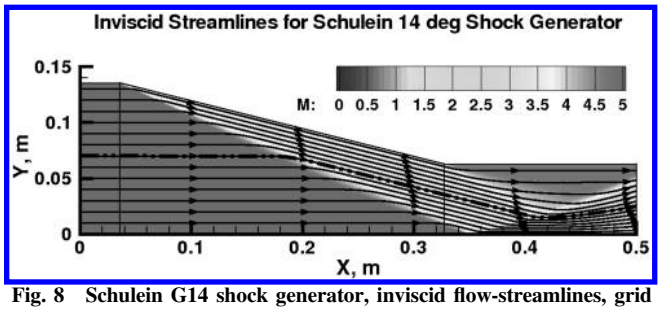

Fig. 8 Schulein G14 shock generator, inviscid flow-streamlines, grid sensitivity study.

cells, Fig. 10 is for a medium grid of $1056 \times 3 \times 256$ cells, and Fig. 11 is for a fine grid of $2112 \times 3 \times 512$ cells. Also shown in these plots is the analytical value $P_{T,2}/P_{T,1} \approx 0.73175$ for the single initial oblique shock generated by the 14 deg inclined shock generator. The coarse grid yields ≈4% error in $P_{T,2}/P_{T,1}$, the medium grid yields ≈1% error in $P_{T,2}/P_{T,1}$, whereas the fine grid yields ≈0.6% error in $P_{T,2}/P_{T,1}$. The error is biased low with too much total pressure loss and related entropy increase. For a coarse grid simulation of a scramjet inlet with as many as 6 oblique shocks, the cumulative error will be as high as $0.96^6 \approx 0.78$ or a 22% error in the primary physical quantity of interest. Clearly this is unacceptable in the presence of multiple strong interactions, and a means of reducing this error source to a tolerable level needs to be found. For this paper, where only single interactions are considered, this is done by grid refinement where required.

In the viscous solutions for the Schulein 10 and 14 deg cases to follow, the primary results presented are computed on "medium" grids. For the Schulein 6 deg viscous case with its significantly weaker shock, the coarse grid was found to be adequate. To ensure acceptable grid convergence, limited "fine" grid solutions were performed, but are shown only for the 14 deg.

C. Experimental SWTBLI Cases

1. Schulein Mach 5, 2D SWTBLI Cases

The experiment provides attached, incipient separation and fully separated impinging SWTBLI cases. In addition to wall pressure and wall heating measurements, Schulein applied redundant techniques to measure experimental wall shear stress for these cases. Also, the pressure measurements, along with the $Q - P^{0.85}$ correlation, provide an indirect redundancy check on the direct wall heating measurements.

These cases are computed using the DPLR Navier–Stokes code with several turbulence models and variations. We consider each case

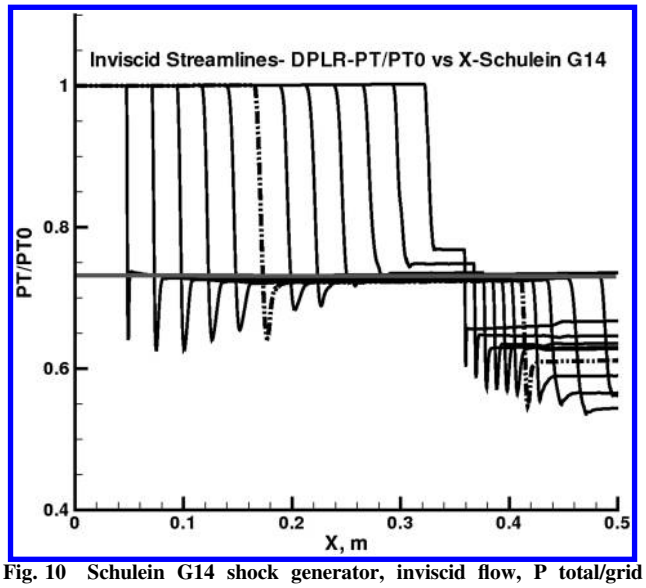

Fig. 10 Schulein G14 shock generator, inviscid flow, P total/grid sensitivity study. Medium grid.

in order, compare CFD with experiment, discuss relevant flow physics and evaluate for each flow case numerical values of uncertainty metrics in this subsection.

a. Schulein 6 deg Attached Case:. For this case, simulations using DPLR and the SST, K-ω and Spalart–Allmaras models were obtained for a $528 \times 3 \times 128$ cell grid, with $y_1^+ \approx 0.05$, and $Re_{\text{Cell}} \approx 0.25$. This case has a much weaker shock system than the 14 deg inviscid problem presented earlier, and limited medium grid results for this case indicate the coarse "128" grid used adequately resolves this shock case. Figures 12–14 depict the wall pressure, wall heating, and wall shear stress variations with x through the interaction region for both the measurements and the CFD results. The CFD wall pressure profiles for all models shown in Fig. 12 compare well with experiment throughout the interaction, also as to shock impingement location. This agreement is reflected in the numerical evaluations for the "peak pressure discrepancy" measure, $\Delta_{P\text{Peak}}$ as defined previously, reported in Table 1. For all the turbulence models used for this case, the pressures were within 2% of experiment.

As a check on the pressure plateau levels in Fig. 12, we perform an inviscid shock analysis. This double-shock inviscid problem for a Mach 5 initial freestream encountering a 6 deg shock generator gives an overall pressure rise of $(P_3/P_1)_{\text{Inv}} = 3.762$ which together with

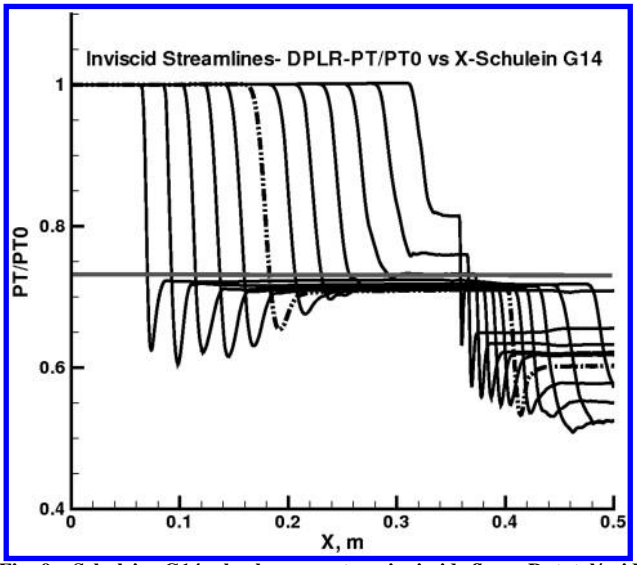

Fig. 9 Schulein G14 shock generator, inviscid flow, P total/grid sensitivity study. "Coarse" grid.

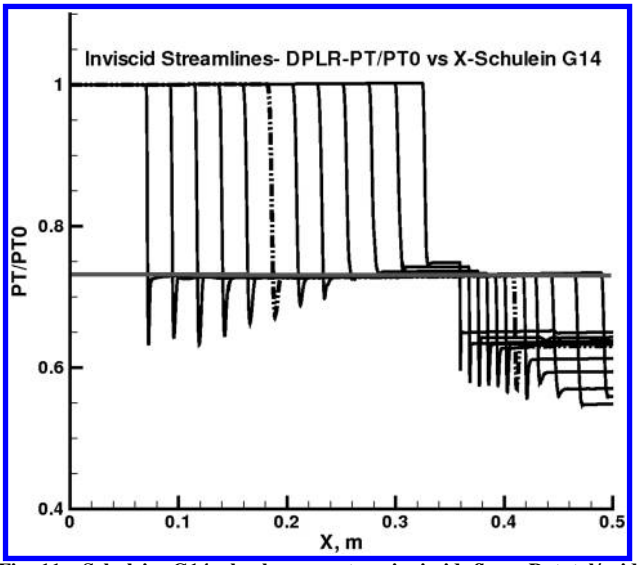

Fig. 11 Schulein G14 shock generator, inviscid flow, P total/grid sensitivity study. Fine grid.

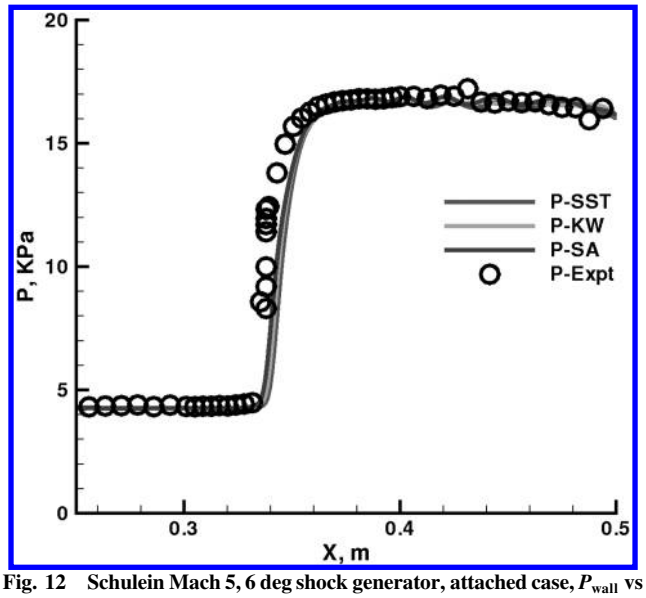

Fig. 12 Schulein Mach 5, 6 deg shock generator, attached case, P_{wall} vs X surface distribution.

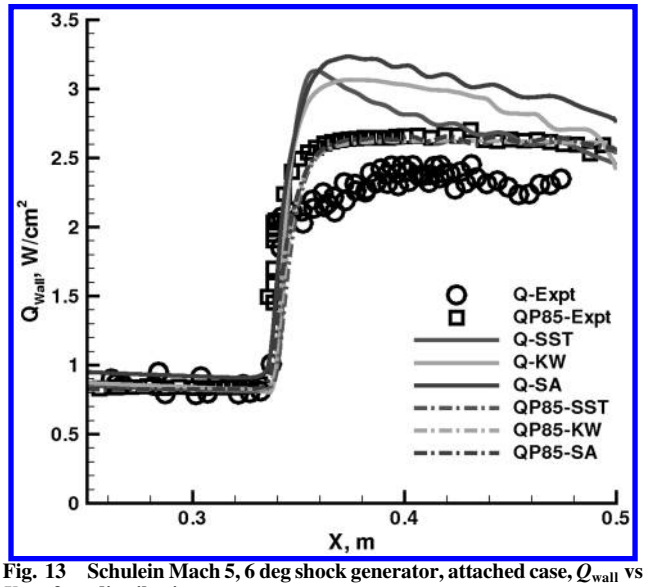

Fig. 13 Schulein Mach 5, 6 deg shock generator, attached case, Q_{wall} vs X surface distribution.

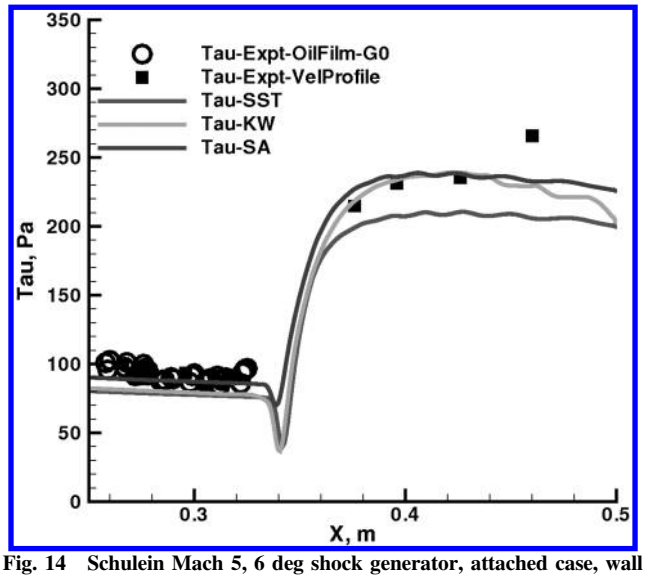

Fig. 14 Schulein Mach 5, 6 deg shock generator, attached case, wall shear stress vs X surface distribution.

Table 1 Uncertainty discrepancy values for Schulein Mach 5, G6, attached case

Model	$\Delta_{\text{Initial}BL,j}$	$\Delta_{LSep,j}$	$\Delta_{PSep,j}$	$\Delta_{QSep,j}$	$\Delta_{PPeak,j}$	$\Delta_{QPeak,j}$
SST	10%	——	——	——	−1.43%	30.20%
K-ω	10%	——	——	——	−1.59%	27.24%
SA	10%	——	——	——	−0.56%	34.56%

the initial pressure of $P_\infty = 4330$ Pa results in a plateau pressure of $P_{\text{Peak,Inv}} = 16,290$ Pa. This inviscid analysis proves about 2% lower than the experiment and the viscous turbulent solutions presented. Although the boundary layer on the shock generator actually brings about a slightly larger apparent shock generator angle, this simple analytical check lends added credibility to both the experiment and the CFD results for pressure.

The pressure plateau region is initiated by the impinging shock followed by the reflection shock. The expansion fan emanating from the trailing edge of the shock generator then weakens the reflection shock, and eventually lowers the pressure terminating the pressure plateau region. The thin boundary-layer thickness for the Schulein experiment establishes the extended distance over which the interaction presents itself, and the long length of the shock generator relative to the boundary-layer thickness, $L_g/\delta_0 \approx 1000$, provides spatial extent between these distinct flow topology features, thereby leading to the extended region of the constant pressure plateau. These arguments justify applying the inviscid double-shock analysis to this case, and also to the remaining Schulein cases, but not to the Murray cases nor to the Kussoy and Horstman cases, which have a much shorter shock generator relative to their boundary-layer thickness.

Figure 13 provides comparisons of experimental wall heating measurements, wall heating CFD results for the three turbulence models, and wall heating derived from wall pressure measurements using the $Q \approx P^{0.85}$ correlation. Wall heating as derived from the $Q \approx P^{0.85}$ correlation is presented for two reasons: first, to show that the data are consistent with correlations of similar data from a number of previous experiments; and second, to illustrate that CFD practitioners may want to use their computed pressures along with the correlation to provide a better estimate of peak heating in the immediate vicinity of SWTBLIs. In contrast to the wall pressure results, the discrepancy between the simulations and the experimental results for wall heating are in the range of 25–35%, see Table 1. The disagreement between the wall heating measurements and the $Q \approx P^{0.85}$ correlation indicates that the wall heating measurements may have been low for this case, with much better agreement between the CFD results and the wall heating correlation results. Through the shock interaction region, the boundary layer is compressed, leading to an increase in pressure, density as well as affecting the temperature profile. Furthermore, there is a significant reduction in boundary-layer thickness, all of which lead to the observed increase in wall heat transfer. Once the rapid compression process of the interaction is passed, the boundary layer again returns to its gradual growth in thickness, with an attendant decrease in heating through the pressure plateau region. However, the heating level at the beginning of the pressure plateau, being within the immediate vicinity of the shock interaction, should still be approximated by the $Q \approx P^{0.85}$ correlation. Note that the SST heating results appears to approach asymptotically the heating results obtained using the $Q \approx P^{0.85}$ correlation. Regardless, the actual wall heating measurements were used for evaluating the uncertainty measures, Δ_p, reported in Table 1.

Table 2 Uncertainty discrepancy values for Schulein Mach 5, G10, incipient separation case

Model	$\Delta_{\text{Initial}BL,j}$	$\Delta_{LSep,j}$	$\Delta_{PSep,j}$	$\Delta_{QSep,j}$	$\Delta_{PPeak,j}$	$\Delta_{QPeak,j}$
SST	10%	18.42%	−7.61%	−27.17%	−0.06%	37.69%
K-ω	10%	14.47%	−20.14%	−46.39%	0.37%	41.61%
SA	10%	−100.%	−55.32%	−43.98%	−0.07%	24.56%

Table 3 Uncertainty discrepancy values for Schulein Mach 5, G14, full separation case

Model	$\Delta_{\text{Initial}BL,j}$	$\Delta_{L\text{Sep},j}$	$\Delta_{P\text{Sep},j}$	$\Delta_{Q\text{Sep},j}$	$\Delta_{P\text{Peak},j}$	$\Delta_{Q\text{Peak},j}$
SST	10%	−14.29%	−29.46%	−27.66%	−0.27%	44.62%
K-ω	10%	5.71%	−35.31%	−38.17%	−1.19%	28.31%
SA	10%	−28.57%	−19.11%	−6.52%	0.36%	16.05%

Table 4 Uncertainty discrepancy values for Kussoy Mach 8.18, G10, full separation case

Model	$\Delta_{\text{Initial}BL,j}$	$\Delta_{L\text{Sep},j}$	$\Delta_{P\text{Sep},j}$	$\Delta_{Q\text{Sep},j}$	$\Delta_{P\text{Peak},j}$	$\Delta_{Q\text{Peak},j}$
SST	10%	−32.26%	−21.44%	−53.47%	−3.76%	31.01%
K-ω	10%	−53.23%	−27.01%	−19.44%	−2.21%	19.58%
SA	10%	−100.00%	−63.31%	−14.87%	−4.70%	8.74%

Table 5 Uncertainty discrepancy values for Murray Mach 8.9, G4.7, attached case

Model	$\Delta_{\text{Initial}BL,j}$	$\Delta_{L\text{Sep},j}$	$\Delta_{P\text{Sep},j}$	$\Delta_{Q\text{Sep},j}$	$\Delta_{P\text{Peak},j}$	$\Delta_{Q\text{Peak},j}$
SST	10%	——	——	——	−2.21%	−0.03%
K-ω	10%	——	——	——	−2.87%	6.98%
SA	10%	——	——	——	−1.26%	6.15%

In Fig. 14, the wall shear stress distribution from CFD simulations is compared with measurements. Upstream of the interaction, the Spalart–Allmaras wall shear stress agrees best with these measurements, whereas the SST and K-ω model are about 10% low. This contrasts with the upstream wall heating comparisons where the SST and K-ω results give slightly better agreement with experiment. It seems not possible to match upstream boundary-layer measurements in all regards at the current state of development for these models.

Also in Fig. 14, after reattachment, a plateau in wall shear stress levels exists, whether for CFD or the measurements, corresponding to the plateau region for pressure and heating. In this postinteraction region, the Spalart–Allmaras and the K-ω model results are within 3%, whereas the SST wall shear stress results are about 12% lower than measured.

The "discrepancy parameters," representing normalized numerical differences between CFD simulations and experiment, are accumulated in Tables 1–6 for each of the experimental cases considered in this paper.

b. Schulein 10 deg Incipient Separation Case:. Figures 15–17 give the wall pressure, wall heat transfer, and wall shear stress from the experiment and the computational simulations. Again the three turbulence models (SST, K-ω, and Spalart–Allmaras) are used for the computations. Table 2 presents the numerical evaluations of the uncertainty discrepancy between CFD and experiment for this incipient separation case.

The SST computed results indicates the largest CFD simulation bubble, with the K-ω computed results giving about 1/2 the spatial extent of separation, and the Spalart–Allmaras model computed results indicating little or no separation. The peak pressure plateau level, whether by experimental measurement or by CFD computations of any of the three models agrees within 1% of the pressure plateau level, $P_3/P_1 = 7.63$ or $P3 = 32850$ Pa, as evaluated by means of the inviscid two-shock analysis. The experimental heat transfer measurements appear low relative to the $Q - P^{0.85}$ correlation (≈10%). The SST, K-ω and Spalart–Allmaras computed heat transfer each exhibit a significant overshoot well above the experimental heat transfer at a location past reattachment and at the start of the experimental peak plateau region. In contrast through the separation bubble region, the turbulence models indicate a drop in wall heating whereas the experiment indicates a slight rise. The overshoot in computed heating and the inability to predict any rise in heat transfer for the separation bubble represent the major contributions to uncertainty for the prediction of these impinging SWTBLI cases. The wall shear stress from the simulations agree with the upstream measurements within ±10%, whereas past reattachment, the SST model appears 10% low, and the K-ω and Spalart–Allmaras being well within the experimental scatter. The SST model agrees quite well with experiment as to the separation extent as indicated by the oil-film measurements and to the actual values of the wall shear stress. The K-ω model separation bubble indicated from computed wall shear stress is slightly smaller than both that of the SST model and the experimental wall shear stress. The Spalart–Allmaras model wall shear stress results for this case do exhibit a drop in wall shear stress due to the shock impingement but without any indication of separation.

c. Schulein 14 deg Full Separation Case:. Grid convergence studies were conducted for this viscous case, using both a fine and a medium grid, and are presented in this section. The uncertainty results presented in Table 3 are from a design-relevant medium grid, with 256 cells between the flat plate and the shock generator, having initial spacing off the wall chosen to provide $y_1^+ \approx 0.05$ and $Re_{\text{Cell}} \approx 0.25$. Transition is specified at $x = 0.1$ m from the leading edge, where $Re_\theta = 500$.

Figures 18–20 depict contour plots for the SST simulations for this case. These contour plots do not show the entire computational domain, but provide an expanded view concentrating on the shock impingement region at about $x = 0.34$ m. Figure 18 depicts U-velocity color contours and Mach number line contours. Figures 19 and 20 provide pressure color contours and temperature color contours, respectively. Flow topology features are seen to be widely separated with the impinging shock originating at the shock generator leading edge, the reflection shocks and the shock generator trailing-edge expansion wave creating distinctly defined inviscid regions of nearly constant Mach number, velocity, pressure and temperature. The separation bubble with its signature λ-shock is clearly identifiable. The boundary layer marked by white contour lines is seen to lift above the separation bubble, then turns back to the surface to close the separation bubble at the reattachment location. Also clearly identified in Figs. 19 and 20 are the regions of elevated pressure and temperature in the inviscid flow just above the boundary layer for the pressure plateau region past reattachment. The inviscid

Table 6 Uncertainty discrepancy values for Murray Mach 8.9, G10, full separation case

Model	$\Delta_{\text{Initial}BL,j}$	$\Delta_{L\text{Sep},j}$	$\Delta_{P\text{Sep},j}$	$\Delta_{Q\text{Sep},j}$	$\Delta_{P\text{Peak},j}$	$\Delta_{Q\text{Peak},j}$
SST	10%	−3.32%	−39.31%	−39.26%	21.52%	20.56%
K-ω	10%	13.38%	−33.95%	−44.83%	16.59%	18.54%
SA	10%	−88.86%	−79.26%	−53.43%	32.90%	39.66%

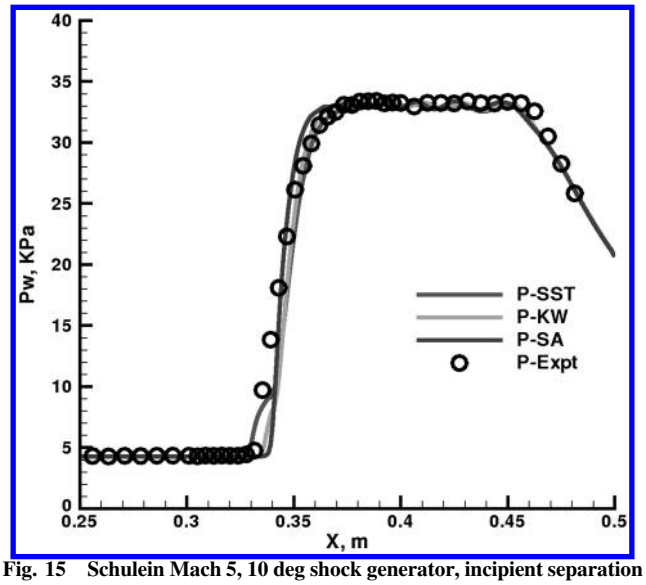

Fig. 15 Schulein Mach 5, 10 deg shock generator, incipient separation case, *P* wall vs *X* surface distribution.

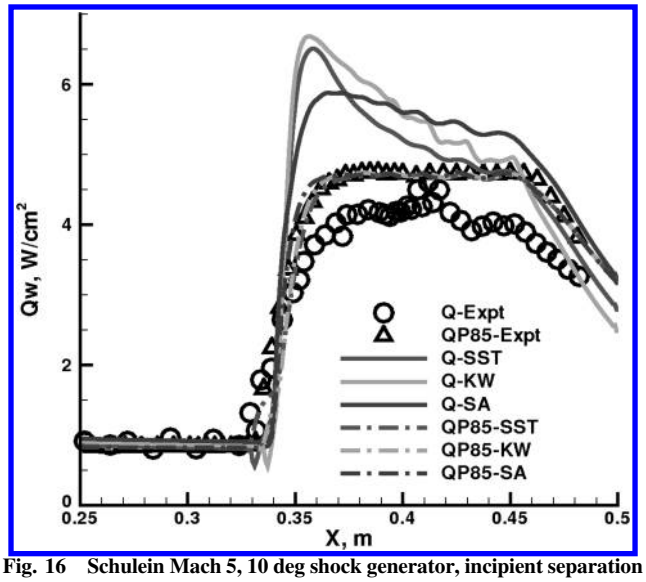

Fig. 16 Schulein Mach 5, 10 deg shock generator, incipient separation case, *Q* wall vs *X*.

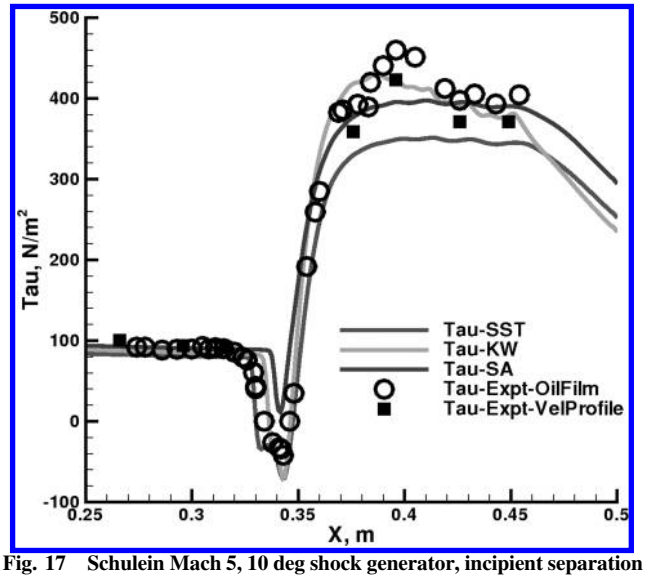

Fig. 17 Schulein Mach 5, 10 deg shock generator, incipient separation case, wall shear stress vs *X*.

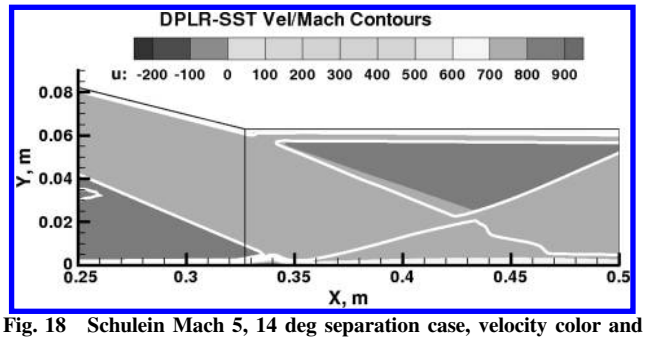

Fig. 18 Schulein Mach 5, 14 deg separation case, velocity color and pressure line contours, separation region.

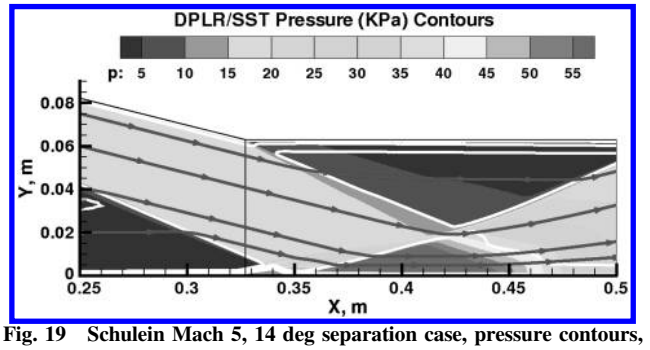

Fig. 19 Schulein Mach 5, 14 deg separation case, pressure contours, separation region.

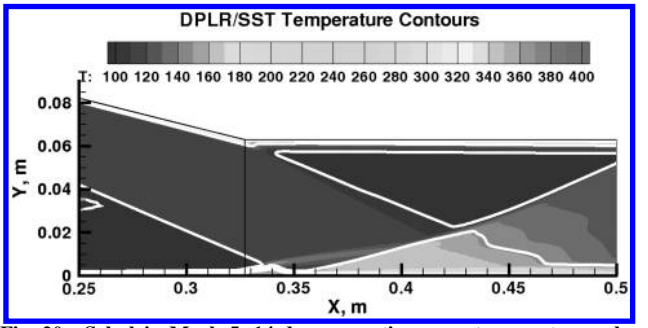

Fig. 20 Schulein Mach 5, 14 deg separation case, temperature color and pressure line contours, separation region.

flow immediately adjacent to the boundary layer for a distance past reattachment is delimited by the reflection shock traveling upwards from reattachment and the expansion wave traveling down from the generator trailing edge. The distance in x between these two flow features allows the extended constant pressure plateau region to develop before being terminated by the shock generator trailing-edge expansion wave. As the extent of the interaction is affected by the initial boundary-layer thickness, and the extent of the pressure plateau region is affected by the distance between the impinging shock generated by the shock generator leading edge and the trailing-edge expansion wave generated by the shock generator trailing edge, then a reasonable nondimensional quantity is the ratio of the shock generator length to the boundary-layer thickness, L_g/δ_0, which for the Schulein experiment is about 1000.

Figures 21–24 show the experimental data compared to the simulations for the three turbulence models. Comparisons with the $Q - P^{0.85}$ correlation are also shown for the reasons explained previously. Table 3 then gives the numerical evaluations of the uncertainty "discrepancy parameter" of the several turbulence models for each respective physical quantity of interest.

In Fig. 21, observed is excellent agreement for all turbulent model results with experiment as to the pressure levels past reattachment and along the peak pressure plateau leading to and including the dropoff where the pressure plateau is terminated by the shock

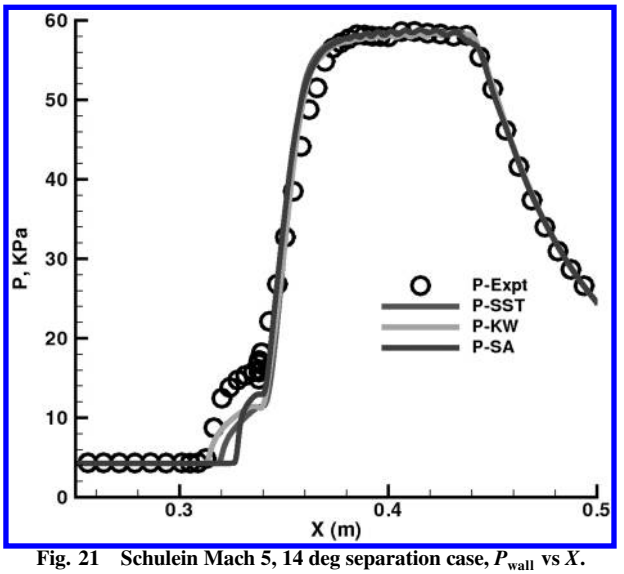

Fig. 21 Schulein Mach 5, 14 deg separation case, P_{wall} vs X.

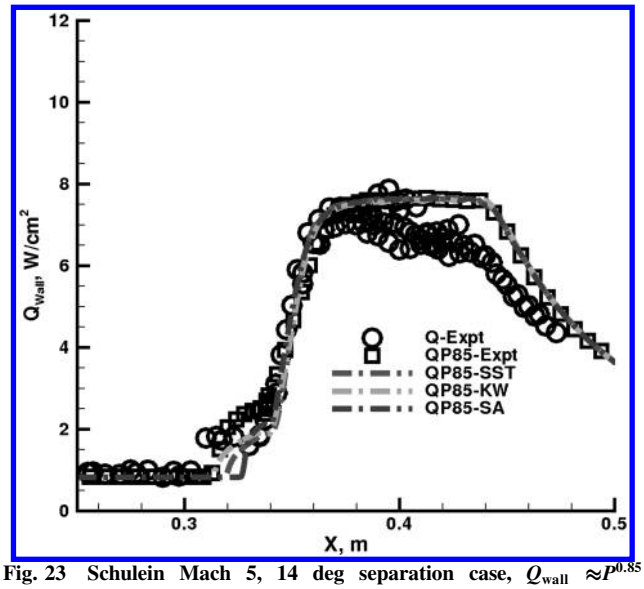

Fig. 23 Schulein Mach 5, 14 deg separation case, $Q_{wall} \approx P^{0.85}$ correlation vs X.

generator trailing-edge expansion fan. Within the separation bubble region, however, generally the turbulence models tend to underpredict the bubble pressure relative to the experimental measurements by about 1/2 or 50%. The extent of the separation bubble pressure region is best predicted by the K-ω model with a slight underprediction, whereas the SST model appears to underpredict the separation extent by 1/4, and the Spalart–Allmaras model underpredicts the separation extent by 1/2. The peak pressure plateau level, whether by experimental measurement or by CFD computations of any of the three models agrees within 1% of the pressure plateau level, $P_3/P_1 = 13.62$ or $P3 = 58675$ Pa, as evaluated by means of the inviscid two-shock analysis described earlier. Further note that the positioning in x as to the location of the pressure rise, an indication of the shock impingement location, agrees quite well between all of the turbulence models and the experiment. As there is no adjustment in x to force this agreement of shock impingement location (nor are there any such shifts in x for any of the solutions presented in this paper), this type of agreement increases credibility of our understanding of the documentation describing the experiment and of the overall solution process.

Figure 22 presents the wall heating results for this fully separated case. Whereas the K-ω heat transfer results are slightly low at the beginning of the interaction, it is the SST model heat transfer results that exhibits a severe spike or overshoot past the reattachment location, just before the region of the experimental pressure and heating peak plateau. The SST model heat transfer peaks at about 50% above the experimental peak value, but does decline toward the plateau level. The Spalart–Allmaras model does not actually exhibit a spiked overshoot in wall heating, but levels off about 25% above the experimental level. In contrast, the K-ω model heating has a moderate overshoot followed by a decline to ≈15% above the experimental heating. A further deficiency in all of the turbulent model results for wall heating is they all show little or no increase in wall heating through the separation bubble region, whereas the experiment shows about a factor of 2 rise above the wall heating of the initial boundary layer.

CFD solutions provided by Gnoffo et al. [3] using a recent implementation of the SST model into the Laura Navier–Stokes code, were conducted on this same grid and are similar to the present results, also showing the postreattachment heating overshoot. Steelant [55] and others also exhibit heating overshoot behavior similar to that of Fig. 22. This similar behavior from different codes suggests that the overshoot seen in Fig. 22 is a feature of the models and not the implementation.

Figure 23 depicts the $Q - P^{0.85}$ correlation based on CFD-computed pressures from the three turbulent models, as well as from the experimental pressures, compared to direct measurements of the experimental heat transfer. Although the $Q - P^{0.85}$ correlation gives

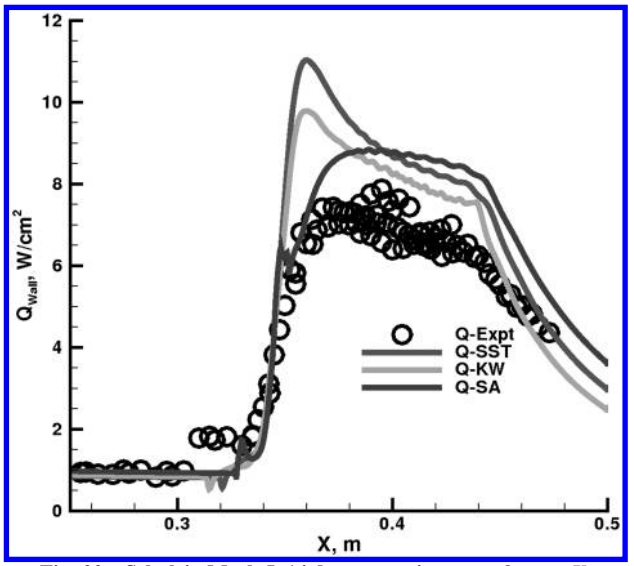

Fig. 22 Schulein Mach 5, 14 deg separation case, Q_{wall} vs X.

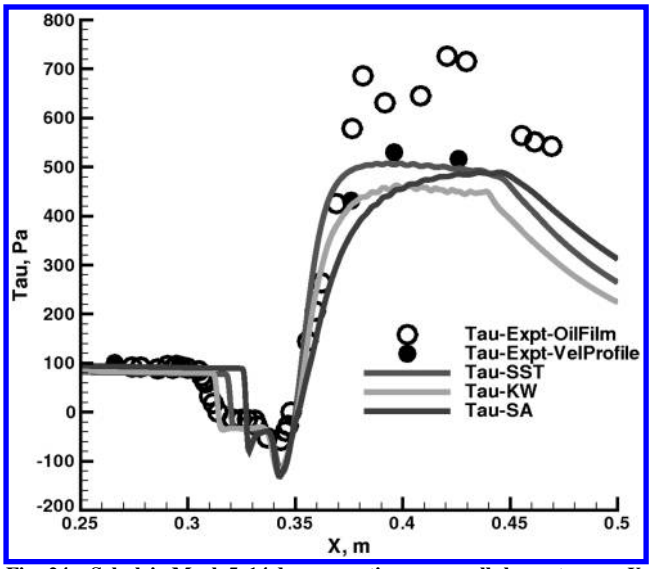

Fig. 24 Schulein Mach 5, 14 deg separation case, wall shear stress vs X.

a nearly constant heating level for the constant pressure region past reattachment, the experimentally measured wall heating achieves its maximum value just past reattachment, then experiences a slight decline with progression along the peak pressure plateau region. As was seen for the 6 and 10 deg cases, this is likely due to the boundary layer, having undergone significant compression and thinning, then returning to its" natural growth response for the nearly zero pressure gradient region past reattachment with an associated gradual decline in wall heating.

Figure 24 provides a comparison of wall shear stress experimentally obtained by two methods, from the oil-film technique and by analysis of the log-law region of pitot probe surveys, with the CFD turbulence model results. There is disagreement between the two experimental approaches on the pressure plateau region; it is believed (by this author) that the oil film may be exhibiting waves in the oil film as a consequence of the high shear stress for the viscosity of oil used for this region leading to instabilities in the oil film. Greater credence is thus given to the pitot-survey derived wall shear stress for the peak pressure plateau region, with both techniques of equal value elsewhere. Although the Spalart–Allmaras model seems to better predict, by a slight degree, the initial boundary layer, the SST model wall shear stress results agree best with experimental results both within the separation bubble and the peak pressure plateau region. The separation bubble extent for the several models relative to experiment as indicated by wall shear stress in this figure was discussed previously for the wall pressure results of Fig. 21.

Figures 25–30 present the results of a study whose purpose was to examine the influence of some of the SST model implementation choices considered in Appendix B, as applied to this separated SWTBLI case.

First examined are the compressibility correction options. Results for SST computations using the CompC.4, CompC.5, and CompC.6 options for the fully separated Schulein case are presented. The $1 - F_1$ modified-Sarkar correction (CompC.4 option) and the $1 - F_1$ modified-Zeman correction (CompC.5 option) do provide a slight increase in extent of the separation bubble, but still underpredict. The $1 - F_1$ modified-Wilcox correction, however, now provides results with an overprediction of the extent of separation. None of these compressibility correction options lead to better agreement as to the underprediction of the separation bubble pressure, nor as to the lack of increase in wall heating for the separation region. The modified-Sarkar and modified-Zeman options do exhibit a slight decrease in the undesirable computed overshoot in postreattachment wall heat transfer, whereas the modified-Wilcox form provides about a 10% decrease in this computed wall heating overshoot.

Next we examine the wall boundary condition options, particularly WallBC1.6. In Appendix B for the Mach 10 boundary layer, the

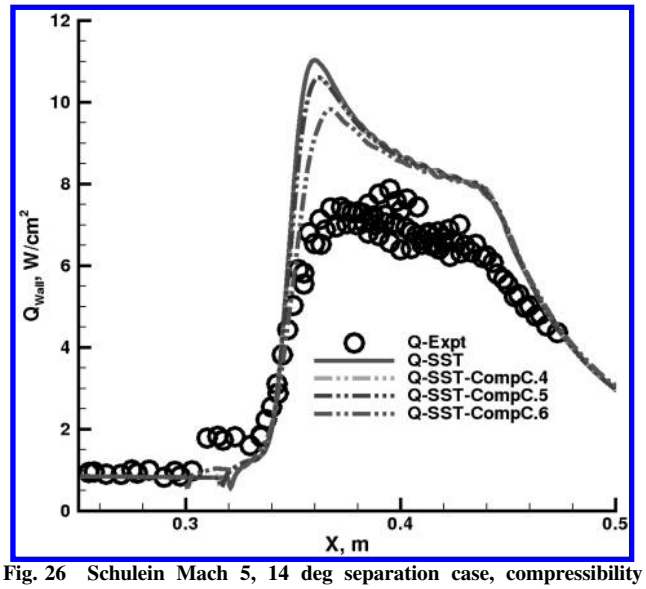

Fig. 26 Schulein Mach 5, 14 deg separation case, compressibility correction study, Q_{wall} vs X.

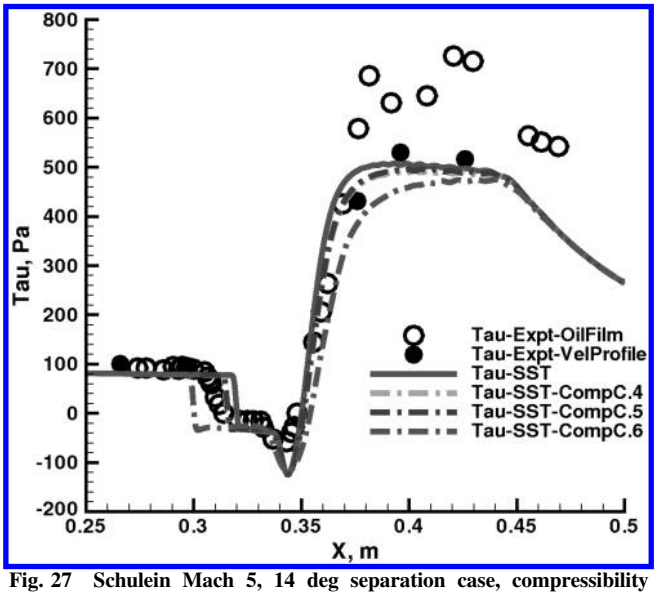

Fig. 27 Schulein Mach 5, 14 deg separation case, compressibility correction study, wall shear stress vs X.

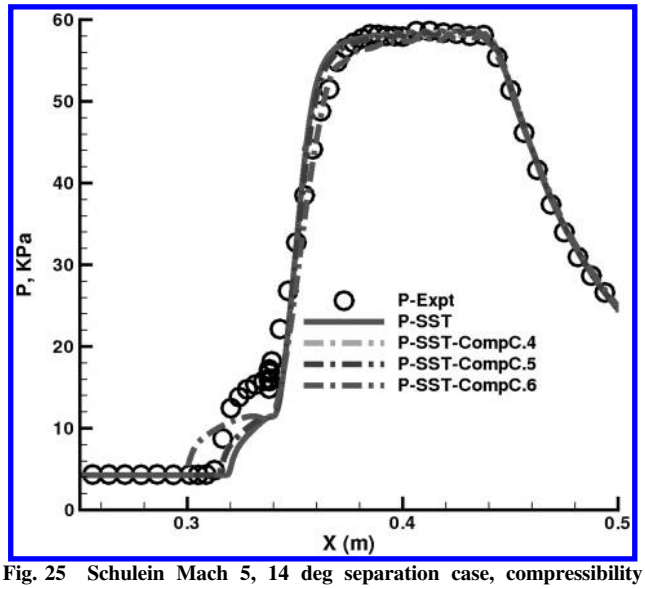

Fig. 25 Schulein Mach 5, 14 deg separation case, compressibility correction study, P_{wall} vs X.

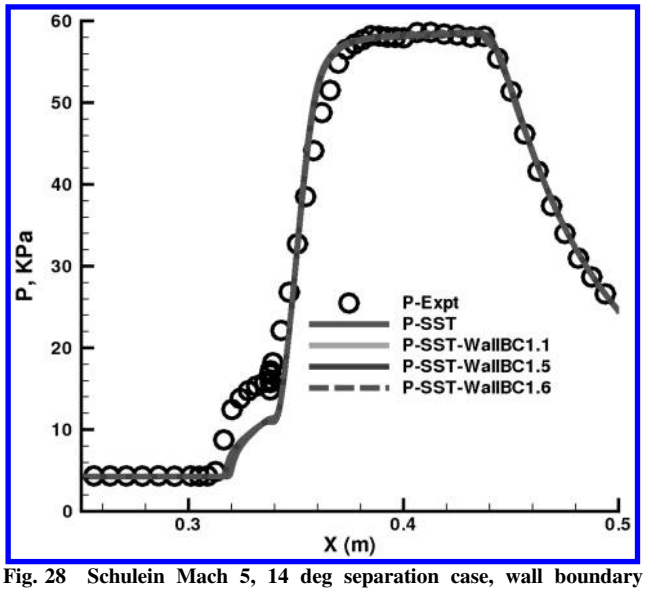

Fig. 28 Schulein Mach 5, 14 deg separation case, wall boundary condition study, P_{wall} vs X.

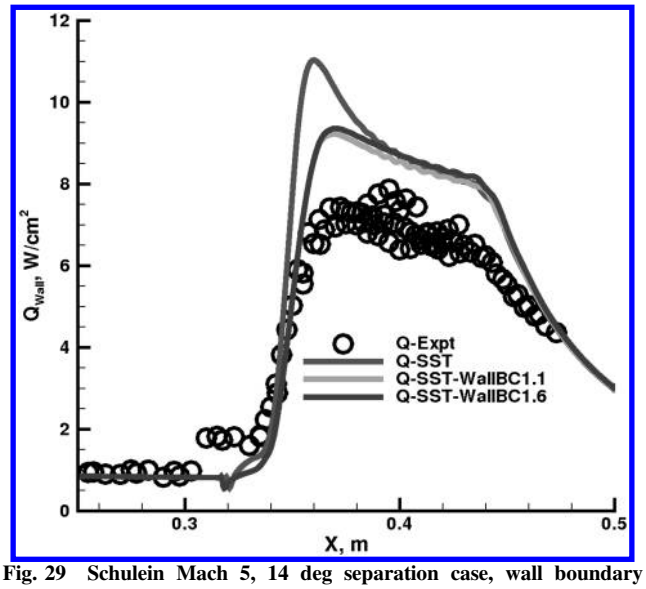

Fig. 29 Schulein Mach 5, 14 deg separation case, wall boundary condition study, Q_{wall} vs X.

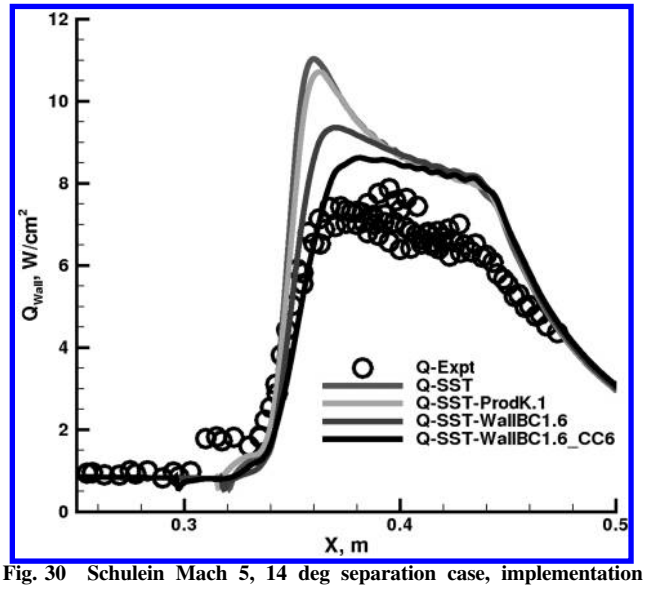

Fig. 30 Schulein Mach 5, 14 deg separation case, implementation study, Q_{wall} vs X.

typical wall boundary condition treatment for the SST model exhibited sensitivity to the initial y^+ spacing, with acceptable results for $y_1^+ < 0.3$. However, wall boundary condition treatments, such as the WallBC1.6 option, that imposed the composite wall sublayer/log-layer analytical expression for ω for those cells closest to the wall up to a value of $y^+ \approx 6$ led to a relatively insensitive response to the initial grid spacing. The WallBC1.6 option completely removes the need for a conventional wall boundary condition; the analytical near wall solution is directly incorporated into the implicit solution procedure for the turbulence variables leading to what might be considered an implicit wall-merging condition. In Figs. 28 and 29 are the pressure and wall-heat transfer distributions for the wall boundary condition treatment study. Only the standard DPLR, the WallBC1 = 1, 5, and 6 options are considered. In Fig. 28, there is little effect of these boundary condition treatments on the SST pressure distribution results. Also, there is no change in separation bubble extent or the underprediction of SST bubble pressure. In Fig. 29, however, both wall boundary condition WallBC1.1 and WallBC1.6 reduce the undesirable overshoot in wall heating to about half of the standard SST turbulence model wall boundary condition treatment. It appears sufficient to implicitly set the ω value for initial cell off the wall to achieve this favorable result. As the WallBC1.6 option also improves grid insensitivity for the SST model, this treatment deserves consideration as the preferred wall treatment. None of the wall boundary condition options, however, appear to favorably affect the underprediction of the separation bubble wall heating, pressure and separation extent.

Figure 30 demonstrates that for the SST model, the DPLR-standard vorticity turbulent production and the "exact" strain-based turbulent production lead to similar wall heating and separation extent. The change in turbulent production form seems to have little effect for this case.

Finally, Fig. 31 gives both the high-density "Seq1" and the medium-density "Seq2" grid SST wall heating results indicating that the results of this section were grid-converged, hence the uncertainty results of Table 3 are based on the more design practical medium-density grid.

2. *Kussoy and Horstman Mach 8.2 2D SWTBLI 10 deg Full Separation Case*

In the 2D shock impingement experiment of Kussoy and Horstman, several wedge angles were used. We concentrate on the full separation 10 deg wedge case. For these computations a five-block grid (four blocks with $96 \times 3 \times 128$ cells and one block of $128 \times 3 \times 32$) was used, with initial grid spacing of $y_1^+ = 0.15$.

Figures 32 and 33 show comparisons of wall pressure and wall heating variation measured through the interaction region with simulations using the three turbulence models. The agreement between the experiment and computation for wall pressure is excellent being within 10%, about the level of experimental uncertainty. The Spalart–Allmaras model agrees to within experimental uncertainty for wall heating as well, although this may be due to fact that the Spalart–Allmaras model does not predict any extent of separation. The SST model (and the implementation variants shown) overpredicts peak heating by 30%, whereas the K-ω model overpredicts peak heating by 20%. Disagreement occurs as to the separation extent, with both the SST and K-ω models underpredicting relative to the experiment. The Spalart–Allmaras model indicates that no separation occurs, whereas the experiment indicates a moderate sized separation bubble. No rise in heat transfer was detected within the separation bubble region for either the computation or the experiment. Further, the SST and K-ω model results differ with the measurements in the separation bubble.

Also seen in Figs. 32 and 33 are results for a select number of implementation options for the SST model. The change in turbulent kinetic energy (TKE) production term to the stress-based (ProdK.1) version makes little impact on the results relative to the standard DPLR approach. However, the use of the free shear compressibility correction with the $(1 - F_1)$ modified version of

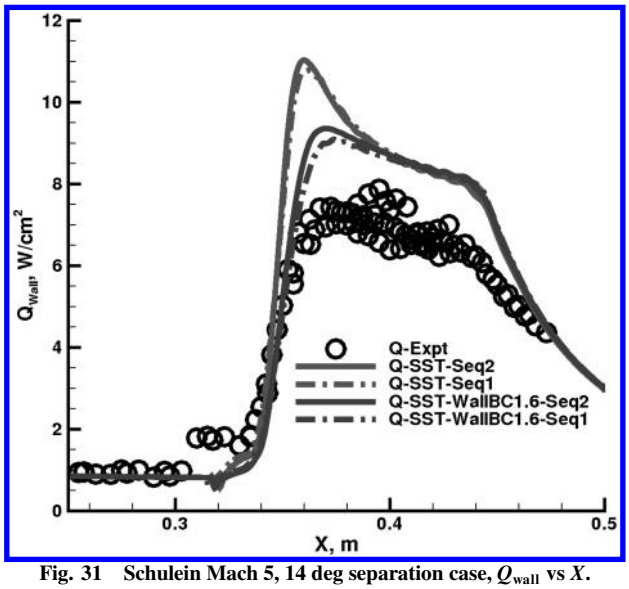

Fig. 31 Schulein Mach 5, 14 deg separation case, Q_{wall} vs X.

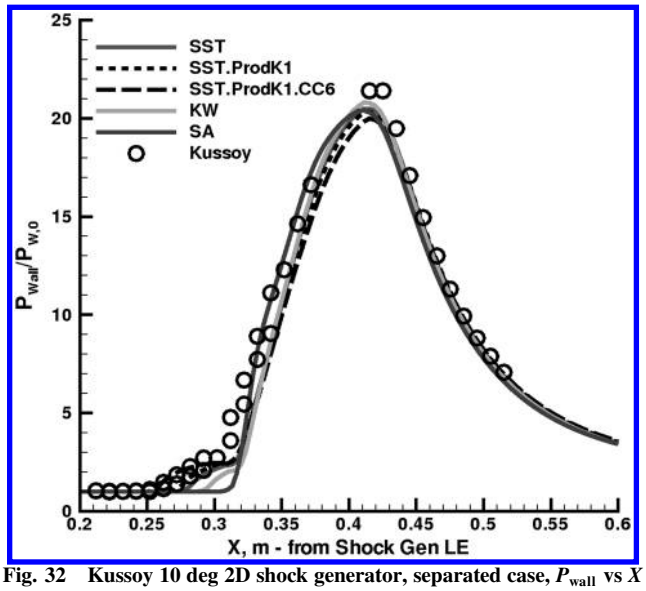

Fig. 32 Kussoy 10 deg 2D shock generator, separated case, P_{wall} vs X surface distribution.

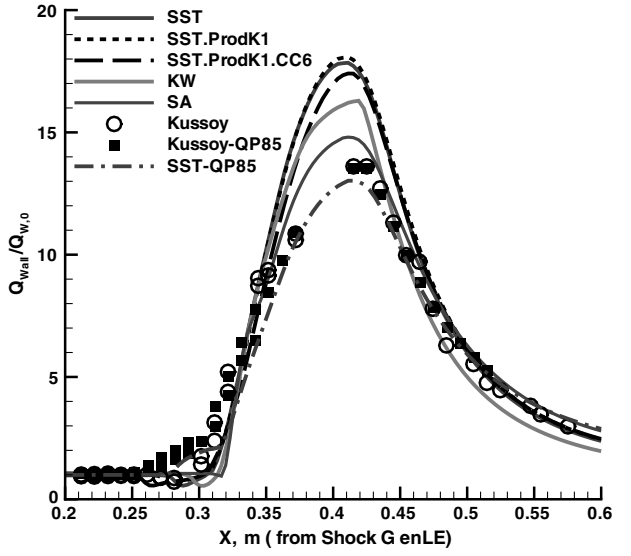

Fig. 33 Kussoy 10 deg 2D shock generator, separated case, Q_{wall} vs X.

Wilcox (CCompC.6) increases the extent of separation so as to better agree with experiment. Regardless, no improvement in wall heating for the separation region is seen by either of these implementation options.

Table 4 gives numerical evaluations for the uncertainty "discrepancy parameters".

3. *Murray Mach 8.9 Axisymmetric SWTBLI Cases*

a. Murray 4.7 deg Attached Case:. Figures 34 and 35 depict the comparison of experiment with DPLR computational results for wall pressure and wall heating for the attached case of the nominal Mach 8.9, impinging SWTBLI experiment of Murray. Figure 36 depicts the wall heating $Q - P^{0.85}$ correlation results for this same case. The shock generator for the attached case is an axisymmetric cowl of 4.7 deg internal angle. The computational grids made use of five blocks with 256 cells between the axisymmetric cylinder and the shock generator. A quarter-plane grid was used for this axisymmetric flow with cells placed every 10 deg. A total of 2,580,470 cells resulted. The initial grid spacing off the cylinder surface was at $y_1^+ \approx 0.01$. General agreement between computation and experiment are excellent as to pressure distribution indicating the geometry is understood and those measures taken to account for the diverging nozzle flow appear to have been successful. There is a slight overprediction of peak pressure, however, it appears to be within the experimental scatter of $\pm 10\%$. There is no extended pressure plateau, likely the result of early termination of any constant pressure region in the inviscid flow above the boundary layer for this region due to the shortness of the shock generator cowl and the generation of an expansion wave at the trailing edge of the cowl leading to early termination of the interaction.

Table 5 gives numerical evaluations for the uncertainty "discrepancy parameters".

b. Murray 10 deg Full Separation Case:. The shock generator is an axisymmetric cowl having a 10 deg internal angle. The simulations were conducted on a five-block grid having 512 cells from the test cylinder to the shock generator, and 1696 cells along the test cylinder length. As the test surface was a cylinder and solutions were made using DPLR3D, cells every 10 deg around the cylinder describe the quarter-plane.

Figures 37 and 38 depict the experimental wall pressure and heating measurements for the fully separated case of the nominal Mach 8.9, impinging SWTBLI experiment of Murray. The wall pressure and heating DPLR computational results for the several turbulence models for this case are also shown in these figures. For

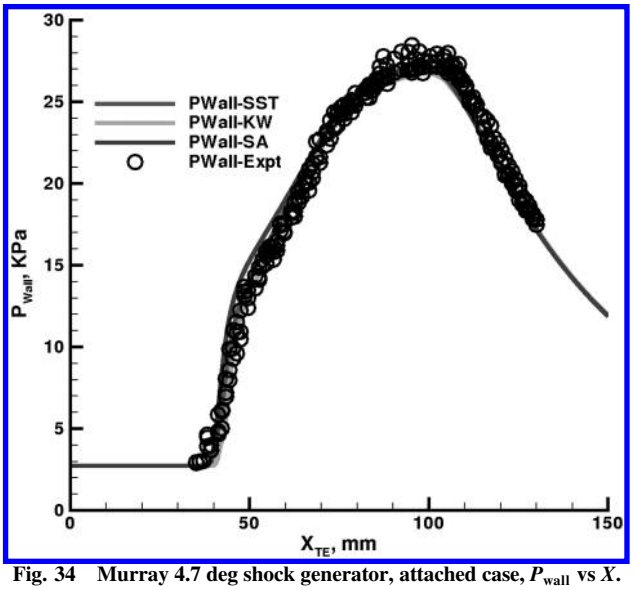

Fig. 34 Murray 4.7 deg shock generator, attached case, P_{wall} vs X.

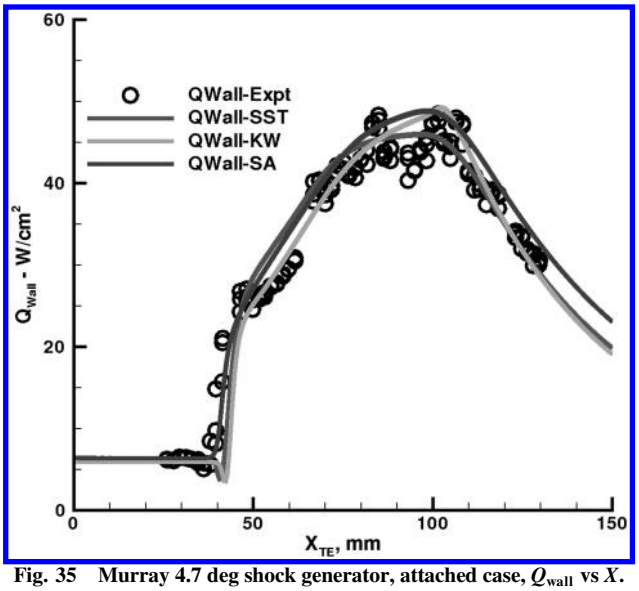

Fig. 35 Murray 4.7 deg shock generator, attached case, Q_{wall} vs X.

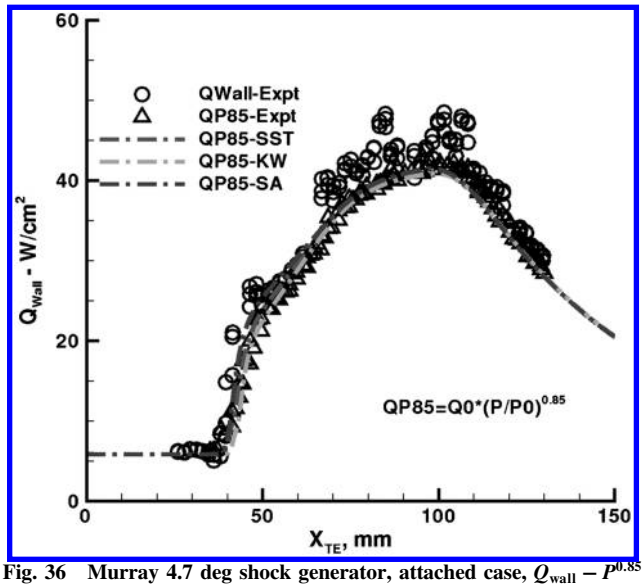

Fig. 36 Murray 4.7 deg shock generator, attached case, $Q_{\text{wall}} - P^{0.85}$ correlation vs X.

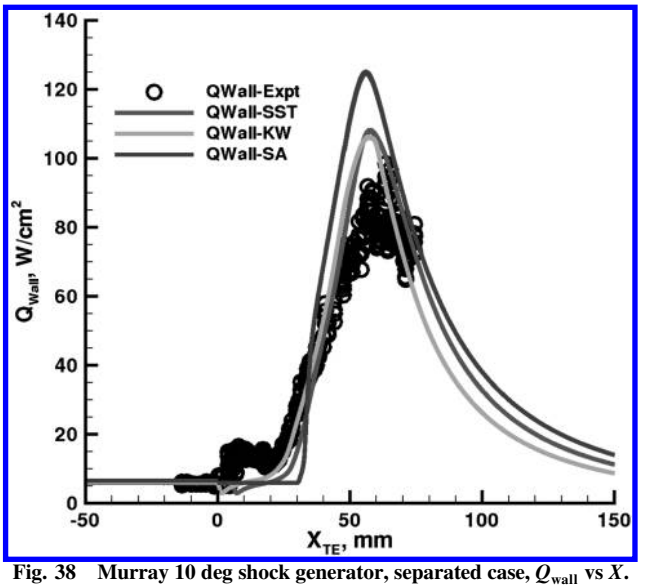

Fig. 38 Murray 10 deg shock generator, separated case, Q_{wall} vs X.

this fully separated case of Murray, there is an overprediction (≈15%) in peak wall pressure past reattachment, and the peak heat transfer is also overpredicted (≈25%). Separation extent is closely predicted by the SST, overpredicted by the K-Omega, whereas Spalart–Allmaras significantly underpredicts. As with the Kussoy and the Schulein experiments, the computations underpredict the wall pressure rise in the separation bubble. Further, although the experiment indicates a heating rise within the separation bubble, none of the turbulence models for the computations so indicate.

The present computations for the separated Kussoy and Murray cases yield reasonable agreement with those experiments for heat transfer, while for the Schulein separated case there exists a severe overshoot in the computed peak heat transfer compared to experiment.

Observe that the Schulein experiment has an extended pressure plateau past reattachment, while a pressure plateau does not occur for either the Kussoy or Murray experiments. Further, the Schulein experiment has a thin initial boundary layer relative to the shock generator length, with $L_g/\delta_0 \approx 1000$. In contrast, both the Kussoy and Murray experiments have a thick initial boundary layer relative to the shock generator length, with $L_g/\delta_0 \approx 110$. The distance required for an interaction of a given strength to "fully develop" will scale as some multiple of the initial boundary-layer thickness, δ_0.

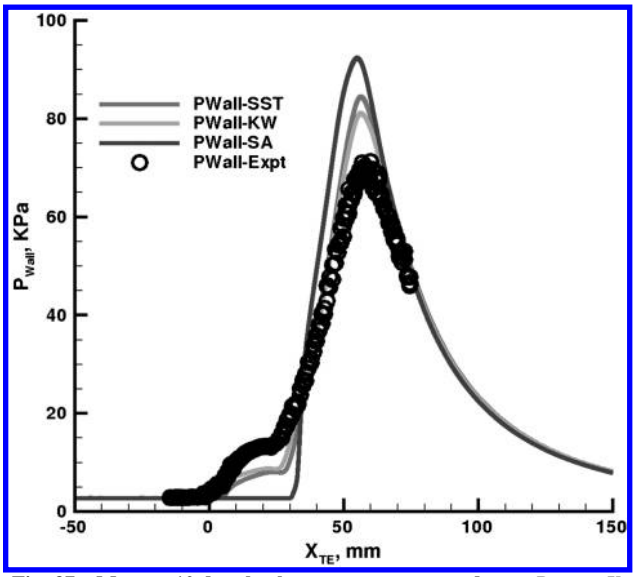

Fig. 37 Murray 10 deg shock generator, separated case, P_{wall} vs X.

However, the distance geometrically available for the interaction to develop is established by the impinging shock initiating the interaction and the expansion fan terminating the interaction. These effects are best measured at the boundary-layer edge, but will scale with the shock generator length, L_g. If the geometrically available interaction distance exceeds the required distance, then the interaction "fully develops" with any excess leading to an extended pressure plateau. The expansion fan generated at the shock generator trailing edge acts to terminate the extended pressure plateau. Thus, the Schulein separated case is fully developed. However, if the distance geometrically available for the interaction is less than the minimum required interaction distance then the interaction is prematurely terminated just past reattachment, without an extended pressure plateau and the interaction is not fully developed. Both the Kussoy and the Murray separated cases are prematurely terminated and not fully developed. Thus, the heat transfer overshoot occurs in the computation only for the fully developed case of Schulein, but not for the prematurely terminated interactions of Kussoy and Murray. The effect of an expansion fan interacting with the reflection shock near the reattachment point is to reduce overall pressure rise allowed to develop (well below idealized two-shock inviscid analysis levels), and thus mitigates overshoot effects in the computations. For the "fully developed" case of Schulein, pressures reach the two-shock inviscid analysis level, the expansion fan is not felt till the end of the extended pressure plateau, far removed from reattachment, and the overshoot in computed heating results just past reattachment.

Figures 39 and 40 provide results for the $Q - P^{0.85}$ correlation for this case and for wall shear stress results from our CFD simulations. Observed in Fig. 39 is that the correlation provides wall heat transfer comparable to the CFD results having a slightly higher level than the direct measurements. From Fig. 40, the wall shear stress results facilitate identification of separation extent, yielding additional information useful for our process of accumulating uncertainty statistics.

Table 6 gives numerical evaluations for the uncertainty "discrepancy parameters".

D. Uncertainty Analysis

The "discrepancy parameters" defined earlier are numerically tabulated for each case in Tables 1–6, with statistical analysis results summarized in Tables 7–9. These summary tables clearly indicate large bias and variance in CFD simulations relative to experiment for hypersonic impinging SWTBLIs.

Also, earlier in this paper, uncertainty measures were defined, (e.g., the peak pressure discrepancy, $\Delta_{Qp} \equiv ((Q_P/Q_0)_{\text{CFD}} - (Q_P/Q_0)_{\text{Exp}})/((Q_P/Q_0)_{\text{Exp}})$), as the difference between CFD and experiment for physics quantities of interest to be evaluated for

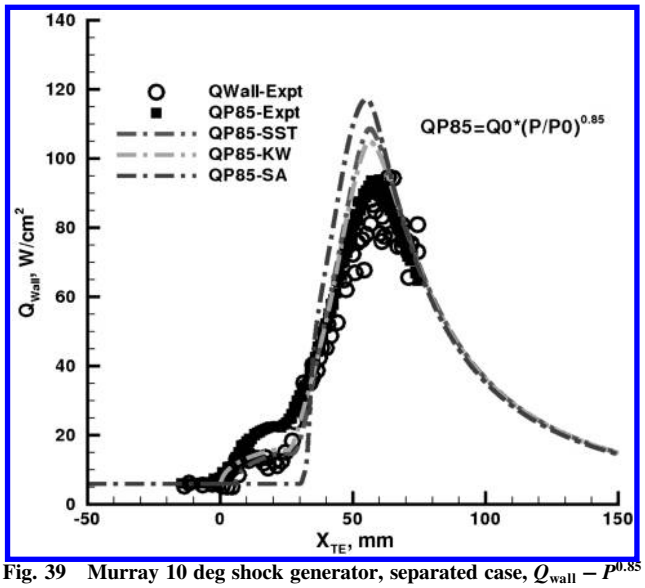

Fig. 39 Murray 10 deg shock generator, separated case, $Q_{\text{wall}} - P^{0.85}$ correlation vs X.

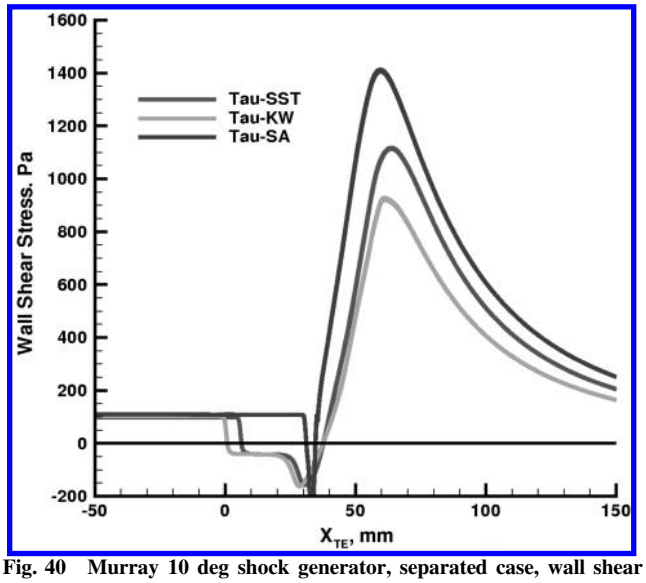

Fig. 40 Murray 10 deg shock generator, separated case, wall shear stress vs X.

each CFD simulation of an experimental case with each of the various turbulence models. Both CFD and experiment contain errors, but an effort has been made to reduce systemic errors, and it is uncertainty in the form of turbulence model deficiencies that predominate.

In Tables 1–6, the numerical evaluations of these discrepancy parameters are accumulated for each experimental case for each of the physics quantities of interest and for each turbulence model. Using these numerical values as raw data for standard statistical analysis, the Uncertainty Tables 7–9 were constructed, which lead to discrepancy parameter means, variances and confidence intervals using Student's t-distribution and standard statistical techniques [38]. Table 7 gives the statistics for the "peak pressure discrepancy" for all the cases, whether attached or separated. Table 8 gives the statistics for the peak pressure and peak wall heat transfer, where only attached cases are included. Table 9 gives the statistics with only the separated cases included, for the Discrepancy between CFD and experiment for the peak pressure and wall heating, as well as for the separation bubble pressure and wall heating and the separation extent. All of the uncertainty tables present the means, variances and both 90 and 95% confidence intervals for all discrepancy parameters applicable to the cases considered.

The statistical results of these tables provide an objective measure that confirms what can be easily observed in the various plots comparing CFD and experiment. These tables also have pragmatic significance in aiding a designer in setting design margins. For example, using the SST model for separated cases, Table 9 indicates that the CFD results for peak heat transfer tend to be 33.5% high, but with a variance of 10.2%, which with design margins based on a 95% confidence level, the expectation is that CFD results might overpredict peak heat transfer by as little as 17.2% or overpredict by as much as 49.8%. These results may well affect how much thermal protection mass should be used to protect surfaces. Needless to say, to know what table to use requires knowledge of separation extent, which itself is subject to uncertainty, because according to Table 9, the SST turbulence model tends to underpredict the separation extent by as much as −41.6% or overpredict by as much as 25.9%.

Similar results can be taken from these tables for the several models, and for the other physics quantities of interest. Note that an underprediction of either peak pressure or separation bubble pressure might well have aerodynamic significance in affecting control surface effectiveness or establishing the substructure strength needed to support external surface panels.

A simple notion is that prediction bias can be *calibrated* and analysis results thereby corrected. In this case, the statistics arrived at for these standard turbulence models suggest that they exhibit not just bias, but considerable variance in their estimates. Bias can be calibrated out of an analysis procedure, but inconsistency of a model cannot. An attempt at calibration correction where the models are not

Table 7 Uncertainty analysis by physical quantity of interest: peak pressure, all cases

Model	$\hat{\mathcal{D}}_{P_p}$	$\hat{\mathcal{D}}'_{P_p}$	90% Conf. Interval $\hat{\mathcal{D}}_{P_p}$	95% Conf. Interval $\hat{\mathcal{D}}_{P_p}$
SST	−1.6%	1.5%	$-3.0\% < \mu_{\text{CFD-Exp}} < -0.1\%$	$-3.4\% < \mu_{\text{CFD-Exp}} < \mathbf{0.3}\%$
KW	−1.5%	1.2%	$-2.7\% < \mu_{\text{CFD-Exp}} < -0.3\%$	$-3.0\% < \mu_{\text{CFD-Exp}} < 0.0\%$
SA	−1.3%	2.0%	$-3.2\% < \mu_{\text{CFD-Exp}} < 0.7\%$	$-3.8\% < \mu_{\text{CFD-Exp}} < 1.3\%$

Table 8 Uncertainty analysis by physical quantity of interest: attached cases

Model	$\hat{\mathcal{D}}$	$\hat{\mathcal{D}}'$	90% Conf. Interval	95% Conf. Interval
	$\hat{\mathcal{D}}_{P_p}$	$\hat{\mathcal{D}}'_{P_p}$	$\hat{\mathcal{D}}_{P_p}$	$\hat{\mathcal{D}}_{P_p}$
SST	−0.50%	0.81%	$-1.86\% < \mu_{\text{CFD-Exp}} < 0.87\%$	$-2.51\% < \mu_{\text{CFD-Exp}} < \mathbf{1.51}\%$
KW	−0.41%	1.04%	$-2.16\% < \mu_{\text{CFD-Exp}} < 1.35\%$	$-2.99\% < \mu_{\text{CFD-Exp}} < 2.18\%$
SA	−0.21%	0.31%	$-0.72\% < \mu_{\text{CFD-Exp}} < 0.30\%$	$-0.97\% < \mu_{\text{CFD-Exp}} < 0.55\%$
	$\hat{\mathcal{D}}_{Q_p}$	$\hat{\mathcal{D}}'_{Q_p}$	90% Conf. Interval $\hat{\mathcal{D}}_{Q_p}$	95% Conf. Interval $\hat{\mathcal{D}}_{Q_p}$
SST	22.6%	20.0%	$-11.1\% < \mu_{\text{CFD-Exp}} < 56.3\%$	$-27.0\% < \mu_{\text{CFD-Exp}} < \mathbf{72.2}\%$
KW	25.4%	17.4%	$-4.0\% < \mu_{\text{CFD-Exp}} < 54.7\%$	$-17.9\% < \mu_{\text{CFD-Exp}} < 68.6\%$
SA	21.8%	14.4%	$-2.5\% < \mu_{\text{CFD-Exp}} < 46.1\%$	$-14.0\% < \mu_{\text{CFD-Exp}} < 57.6\%$

Table 9 Uncertainty analysis by physical quantity of interest: separation cases

Model	$\hat{\mathcal{D}}$	$\hat{\mathcal{D}}'$	90% Conf. Interval	95% Conf. Interval
	$\hat{\mathcal{D}}_{Pp}$	$\hat{\mathcal{D}}'_{Pp}$	$\hat{\mathcal{D}}_{Pp}$	$\hat{\mathcal{D}}_{Pp}$
SST	−1.36%	2.08%	$-4.87\% < \mu_{\text{CFD-Exp}} < 2.14\%$	$-6.53\% < \mu_{\text{CFD-Exp}} < \mathbf{3.80}\%$
KW	−1.01%	1.30%	$-3.20\% < \mu_{\text{CFD-Exp}} < 1.18\%$	$-4.24\% < \mu_{\text{CFD-Exp}} < 2.22\%$
SA	−1.47%	2.81%	$-6.20\% < \mu_{\text{CFD-Exp}} < 3.26\%$	$-8.44\% < \mu_{\text{CFD-Exp}} < 5.50\%$
	$\hat{\mathcal{D}}_{Qp}$	$\hat{\mathcal{D}}'_{Qp}$	90% Conf. Interval $\hat{\mathcal{D}}_{Qp}$	95% Conf. Interval $\hat{\mathcal{D}}_{Qp}$
SST	33.5%	10.2%	$21.4\% < \mu_{\text{CFD-Exp}} < 45.5\%$	$17.2\% < \mu_{\text{CFD-Exp}} < \mathbf{49.8}\%$
KW	27.0%	10.7%	$14.5\% < \mu_{\text{CFD-Exp}} < 39.6\%$	$10.0\% < \mu_{\text{CFD-Exp}} < 44.0\%$
SA	22.3%	13.3%	$6.6\% < \mu_{\text{CFD-Exp}} < 37.9\%$	$1.1\% < \mu_{\text{CFD-Exp}} < 43.4\%$
	$\hat{\mathcal{D}}_{Pb}$	$\hat{\mathcal{D}}'_{Pb}$	90% Conf. Interval $\hat{\mathcal{D}}_{Pb}$	95% Conf. Interval $\hat{\mathcal{D}}_{Pb}$
SST	−24.5%	13.4%	$-40.2\% < \mu_{\text{CFD-Exp}} < 8.7\%$	$\mathbf{-45.8}\% < \mu_{\text{CFD-Exp}} < -3.1\%$
KW	−29.1%	7.0%	$-37.3\% < \mu_{\text{CFD-Exp}} < -20.9\%$	$-40.2\% < \mu_{\text{CFD-Exp}} < -18.0\%$
SA	−54.3%	25.5%	$-84.2\% < \mu_{\text{CFD-Exp}} < -24.3\%$	$-94.7\% < \mu_{\text{CFD-Exp}} < -13.8\%$
	$\hat{\mathcal{D}}_{Qb}$	$\hat{\mathcal{D}}'_{Qb}$	90% Conf. Interval $\hat{\mathcal{D}}_{Qb}$	95% Conf. Interval $\hat{\mathcal{D}}_{Qb}$
SST	−36.9%	12.4%	$-51.5\% < \mu_{\text{CFD-Exp}} < -22.3\%$	$\mathbf{-56.6}\% < \mu_{\text{CFD-Exp}} < -17.2\%$
KW	−37.2%	12.4%	$-51.8\% < \mu_{\text{CFD-Exp}} < -22.7\%$	$-56.9\% < \mu_{\text{CFD-Exp}} < -17.5\%$
SA	−29.7%	22.5%	$-56.2\% < \mu_{\text{CFD-Exp}} < -3.2\%$	$-65.6\% < \mu_{\text{CFD-Exp}} < 6.2\%$
	$\hat{\mathcal{D}}_{Ls}$	$\hat{\mathcal{D}}'_{Ls}$	90% Conf. Interval $\hat{\mathcal{D}}_{Ls}$	95% Conf. Interval $\hat{\mathcal{D}}_{Ls}$
SST	−7.9%	21.2%	$-32.8\% < \mu_{\text{CFD-Exp}} < 17.1\%$	$\mathbf{-41.6}\% < \mu_{\text{CFD-Exp}} < 25.9\%$
KW	−4.7%	31.9%	$-42.3\% < \mu_{\text{CFD-Exp}} < 32.9\%$	$-55.5\% < \mu_{\text{CFD-Exp}} < 46.2\%$
SA	−79.4%	34.3%	$-120.0\% < \mu_{\text{CFD-Exp}} < -39.9\%$	$-134.0\% < \mu_{\text{CFD-Exp}} < -24.8\%$

just inaccurate, but also inconsistent, would have to be considered unreliable.

From Tables 7–9 can be seen that at the present state of art for these turbulence models, simulations can be expected to have 95% confidence intervals with at least one bound reaching as high as 50%. The SST and K-ω models exhibit similar statistics, with wall heating being the most problematic. Peak pressures are reasonably predicted with statistics for the SST and K-ω models signifying confidence interval limits of ≈10%. The separation bubble pressures and wall heating are significantly underpredicted for all models, suggesting considerable work needs to be done to improve predictive capability in this area. The Spalart–Allmaras results exhibit a consistent tendency to resist separation, with $\approx -100\%$ separation bubble length "discrepancy parameter" statistics for the separation cases.

An important realization is that engineering analysis methods (based on correlations) may prove fully competitive and/or complementary to high-fidelity physics-based RANS-based methods. Table 10 explores such an alternative engineering approach, suggested by considering the many wall heating plots, aimed at improving impinging SWTBLI peak heating analysis. For this indirect approach, the $Q - P^{0.85}$ correlation is applied to CFD-SST wall pressures to obtain estimates for wall heating in the vicinity of the interaction rather than directly relying on CFD wall heating. Similar to discrepancy statistics for the high-fidelity CFD based $\hat{\mathcal{D}}_{Qp}$ of Table 7–9, the discrepancy statistics $\hat{\mathcal{D}}_{QP85}$ for this new wall heating estimator are then tabulated in Table 10 for the SWTBLI cases and for the separated cases. This hybrid approach yields significant improvement, for example, in the separated cases, primarily in an unbiased mean for the hybrid $QP85$ approach with $\hat{\mathcal{D}}_{QP85} \approx 7.84\%$ in Table 10 compared to $\hat{\mathcal{D}}_{Qp} \approx 33.5\%$ in Table 9 for the high-fidelity CFD-SST approach. Similar variances are observed, however, with $\hat{\mathcal{D}}'_{QP85} \approx 12\%$ in Table 10 for the hybrid approach compared to $\hat{\mathcal{D}}'_{Qp} \approx 10$–$13\%$ in Table 9 for the high-fidelity CFD-SST approach. The confidence intervals for this alternative approach are also improved over the direct CFD approach. The current status of turbulence modeling for impinging SWTBLIs is clearly better for wall pressure results than for wall heating, suggesting a need for focused modeling improvement efforts.

In physical modeling of turbulence a goal should be consistent accuracy, with both minimal bias and variance. High levels of bias and variance indicate more than that a model is inaccurate, but may also indicate a misleading trend response of that model to parametric perturbations. This latter effect can be catastrophic to design optimization attempts. We know from free interaction theory [14,15] and from physics-based correlations [16], albeit mostly obtained at lower Mach number, what the general effect on separation with variations in the free interaction parameters (Mach number, Reynolds number, shock strength, and levels of wall cooling) should be. A plausible explanation for the large variances in the discrepancy parameters for the turbulence models in the current study may lay more in random positioning of the available experiments in free interaction parameter space, coupled with incorrect trend response of the turbulence models to variations in free interaction parameters, rather than random responses of the turbulence modeling. This may also account for the common experience in turbulence assessments, where one model is found "best" for one experiment, while a second model is best for another experiment.

The simple approach taken of computing single experiments and then assessing results can be misleading in that approach hides the effect of known trends on the physics of SWTBLI. A better approach would seem to evaluate turbulence models using a number of experiments that adequately sample the applicable parameter space. Good experimental design, and computational validation, should include moderate perturbations off-condition to provide an opportunity for "trend analysis" with variation of these separate effects around baseline conditions. More complete knowledge of parametric trend behavior, both of the simulation physics model and of the measured experiments, potentially provide both the modeler and the system design optimization process with additional information that lead to better models and better designs.

Furthermore, the present approach of accumulating and evaluating statistics on the discrepancy between computations and experiment

Table 10 Uncertainty analysis for hypersonic impingement SWTBLI peak heating by hybrid CFD-SST/$QP85$ correlation method

SWTBLI type	$\hat{\mathcal{D}}_{Qp85}$	$\hat{\mathcal{D}}'_{Qp85}$	90% Conf. Interval $\hat{\mathcal{D}}_{Qp85}$	95% Conf. Interval $\hat{\mathcal{D}}_{Qp85}$
All	5.24%	12.1%	$-4.7\% < \mu_{QP85\text{-Exp}} < 15.2\%$	$-7.4\% < \mu_{QP85\text{-Exp}} < \mathbf{17.9}\%$
Sep	7.84%	11.9%	$-6.2\% < \mu_{QP85\text{-Exp}} < 21.9\%$	$-11.2\% < \mu_{QP85\text{-Exp}} < \mathbf{26.8}\%$

for a limited number of cases only reveals that there are hidden physics effects not appropriately accounted for in present modeling. A more sophisticated design of experiments where trends about several baseline mean conditions are explored might be more revealing of such model deficiencies, giving the model developer and design optimizer more information to meet their goals. To that end, both Schulein and Kussoy provide further cases, although with less information, and examination of those cases are worth further examination.

That the λ-shock separated regions are highly unsteady is a factor implicitly incorporated into empirical correlations, but is not factored into present-day quasi-steady simulations using RANS codes. The added uncertainty contributed by shock separated unsteadiness could well be a contributor to the large confidence intervals for the separation bubble statistics arrived at in this section. However, even were unsteady shock separation physics to be accurately incorporated into fully validated DES methods, the use of such time-resolved techniques for routine production design or system optimization purposes will prove prohibitively expensive for some time to come.

Clearly there is a motive to improve the turbulence models used for aerospace purposes where inaccurate analysis regarding pressure and heating lead can lead to excessive system mass, whether for thermal protection or structural support, or loss of reliable aerodynamic response, both of which can significantly degrade the potential design. The statistics presented in these tables should provide some focus on specific areas in most need of improvement.

E. "Nominal-Trajectory" Flight Case: Real Gas Sensitivity Study

To investigate the issue of what additional effects might arise in extrapolation of existing ground tests to "flight cases" for scramjet application, typical flight conditions were derived from the published trajectory of Billig [1]. These conditions are given in Table 11, and compared to the test conditions of the experimental ground tests considered in this paper. The geometric configuration chosen was similar to that of Kussoy, but scaled up in size to account for a lengthy run in advance of the interaction. A relative flow angle of −4.5° of the freestream with respect to the flat test surface accounts for a lifting cruise configuration of a scramjet powered vehicle.

The chosen flight conditions were at Mach 7 and 14, and included both an attached (5.5 deg shock generator, not shown in Table 11) and a separated case (10 deg shock generator) representing the impinging shock generated by the top surface of an inlet duct impinging on the bottom test surface of that same inlet duct. DPLR simulations were conducted using air modeled as both a perfect gas and a calorically imperfect/dissociating real gas using the Park five-species air model. The conditions at Mach 7 are close to that of Kussoy, and we do not pursue those further as no oxygen dissociation was observed. However, the Mach 14 separated results exhibits real gas effects, not due to the small degree of dissociation of O_2 for these conditions, but rather as temperatures exceed ≈2219 K where variable specific heat capacity effects for O_2 begin to be encountered.

Figures 41 and 42 provide the wall pressure and wall heat transfer distribution (X is the distance from the shock generator leading edge, and does not include the run length of the test surface preceding the shock generator). Perfect gas and real gas simulation results for both the SST and K-ω models are presented. SST results with frozen chemistry and variable Cp are also shown. There are no data to validate these simulations, so the purpose of these simulations is exploratory and as a limited sensitivity study. Observed in these figures is that the K-ω model gives a larger separation extent than does the SST model, and that the real gas simulations for both models exhibit a reduction in separation extent and to an increase in peak pressure. The effect of variable Cp-frozen chemistry is to decrease separation extent but increase postreattachment heating. As with ground test experimental cases, neither of these models predicts an increase in wall heat transfer for the separation bubble. The real gas simulations results, for both of these models, also show an increase of almost 20% in peak heating past reattachment.

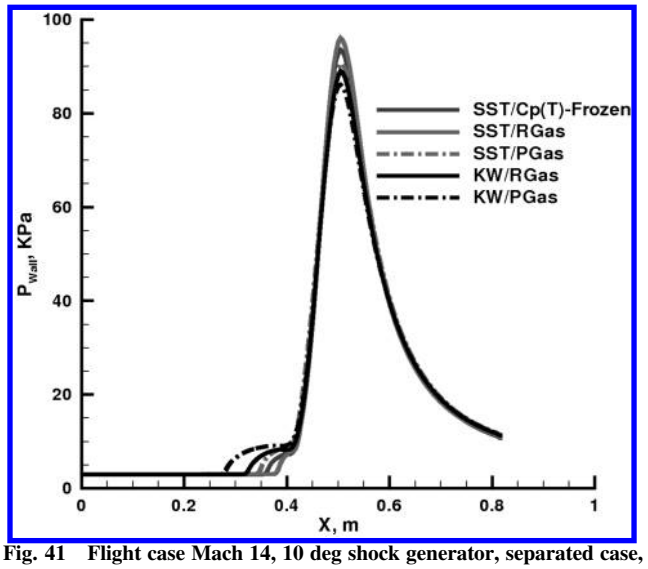

Fig. 41 Flight case Mach 14, 10 deg shock generator, separated case, pressure distribution comparison for SST vs K-ω, real gas vs perfect gas.

To understand better the nature of this real gas effect, Figs. 43 and 44 depict Mach color contours with pressure line contours in white, and streamlines in red. These plots are based on the SST simulations with perfect gas and 5-species chemistry modeling of air, respectively. In both plots, the shock impinges about $X = 0.4$ m and the inviscid regions appear quite similar. A significantly larger separation bubble (seen as the dark blue color contour region) occurs for the perfect gas simulation. Figure 45 depicts temperature color contours for the five-species chemistry modeling of air. The greatest increase in flowfield temperature for these simulations occurs within the boundary layer, reaching 4438 K in the vicinity of shock impingement, but only after reattachment. Figure 46 then provides color contours of the mass fraction of atomic oxygen, indicating the dissociation of molecular oxygen, O_2, into its element form. Most surprising is how little oxygen has actually undergone dissociation, with less than 0.2% mass fraction of atomic oxygen present, leading to the ≈20% increase in peak heat transfer. Further, only a quite small fraction of this atomic oxygen appears within the separation bubble, even though there is a substantial reduction in extent of separation indicated as a consequence of real gas effects. The real gas effect appears to be both that of air being calorically imperfect and of oxygen dissociation.

Table 11 Experimental case nominal condition

Case	Mach	β, deg	P_w:P_T, KPa	T_∞:T_0, K	ρ_∞, Kg/m^3	ReU, m^{-1}	H_0, MJ/Kg
Schulein att air	5.0	6	$P_T = 2120$	$T_0 = 410$	$2.0674 \cdot 10^{-2}$	$37 \cdot 10^6$	0.41
Schulein incsep	5.0	10	$P_T = 2120$	$T_0 = 410$	$2.0674 \cdot 10^{-2}$	$37 \cdot 10^6$	0.41
Schulein fullsep	5.0	14	$P_T = 2120$	$T_0 = 410$	$2.0674 \cdot 10^{-2}$	$37 \cdot 10^6$	0.41
Murray att N_2	8.9	4.7	$P_T = 60000$	$T_0 = 1150$	——	$47.4 \cdot 10^6$	1.1
Murray sep N_2	8.9	10	$P_T = 60000$	$T_0 = 1150$	——	$47.4 \cdot 10^6$	1.1
Kussoy sep air	8.18	10	$P_\infty = 0.430$	$T_0 = 1166$	$1.87 \cdot 10^{-2}$	$7.94 \cdot 10^6$	1.17
Flight M7-sep	7.0	10	——	$T_\infty = 220.94$	$4.401 \cdot 10^{-2}$	$23 \cdot 10^6$	2.4
Flight M14-sep	14.0	10	——	$T_\infty = 246.93$	$9.811 \cdot 10^{-3}$	$10 \cdot 10^6$	9.97

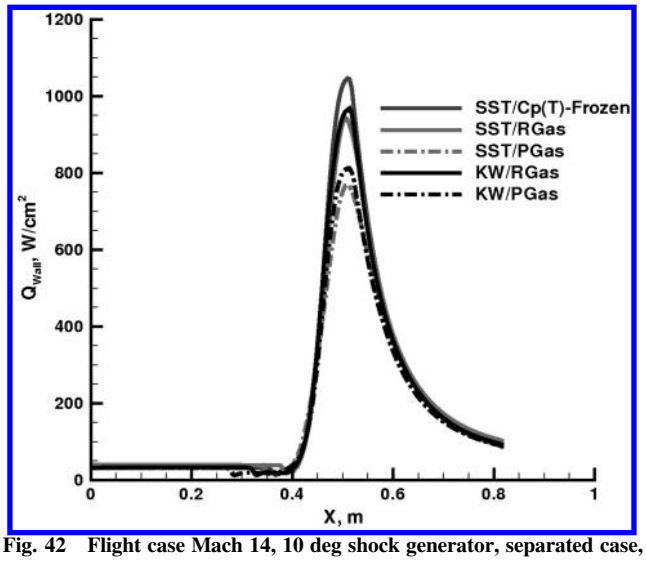

Fig. 42 Flight case Mach 14, 10 deg shock generator, separated case, wall heat transfer distribution comparison for SST vs *K-ω*, real gas vs perfect gas.

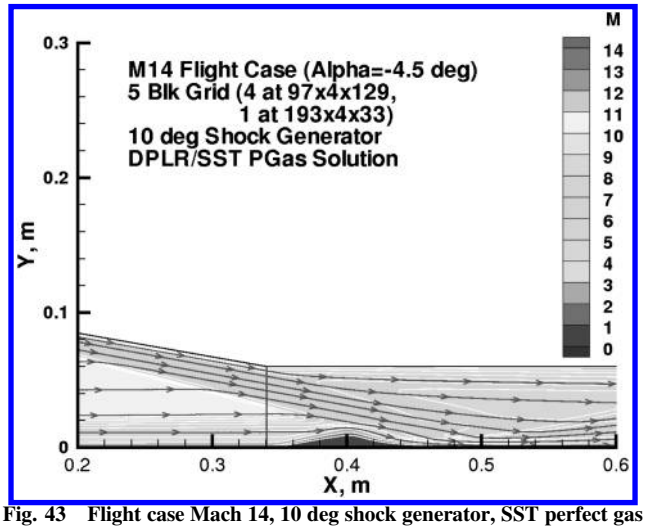

Fig. 43 Flight case Mach 14, 10 deg shock generator, SST perfect gas separated case, Mach color contours *w/* pressure line contours.

Troubling about these "flight case" results is the severity of the simulated real gas effect relies on turbulence modeling in the vicinity of separation and reattachment, which are regions where these models have been demonstrated to exhibit the greatest deficiency in

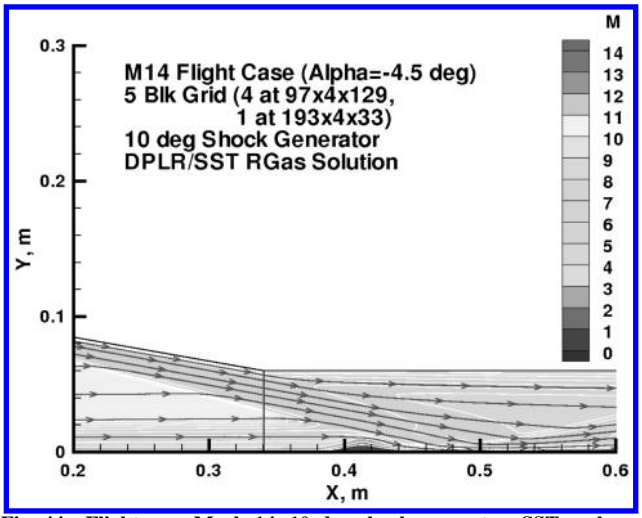

Fig. 44 Flight case Mach 14, 10 deg shock generator, SST real gas separated case, Mach color contours *w/* pressure line contours.

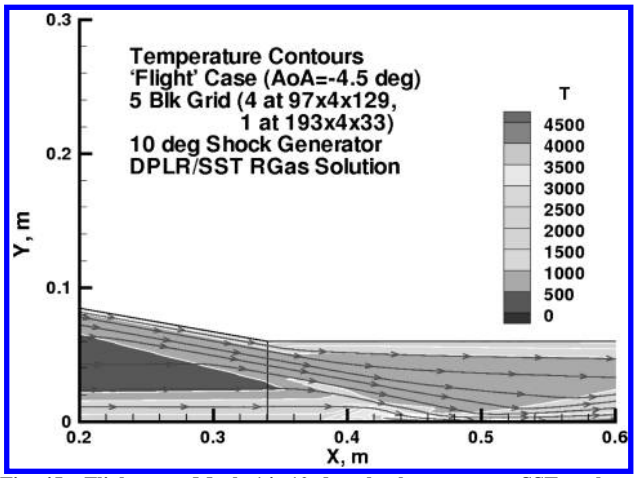

Fig. 45 Flight case Mach 14, 10 deg shock generator, SST real gas separated case, temperature color contours *w/* pressure line contours.

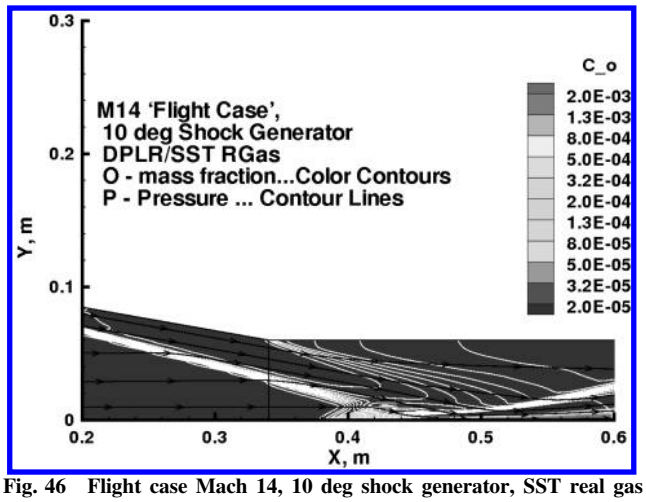

Fig. 46 Flight case Mach 14, 10 deg shock generator, SST real gas separated case, dissociated oxygen-color contours *w* pressure line contours.

their performance. Further troubling is the lack of experiments (although, see Mallinson et al. [62] for a *laminar* high-enthalpy compression corner case) to validate these observations, even qualitatively, in that flow region where the physics modeling is the most uncertain, which compounds the substantial uncertainty the developer of scramjet technology must account for in the design of experimental flights and when relying on CFD based analysis to explore optimized designs.

IV. Summary

Navier–Stokes simulations using the SST, the *K-ω* and the Spalart–Allmaras turbulence models were obtained for three experiments, consisting of six attached and separated cases total. Determination of computational uncertainty for these cases was then evaluated based on definition of uncertainty measures indicating the difference or discrepancy between the computed results and the experiments for as many as five primary physics quantities of interest to either a designer or model developer, i.e., 1) extent of separation (computation versus experiment); 2) postattachment pressure rise (computation versus experiment); 3) postattachment heating rise (computation versus experiment), and if the case is separated, then also 4) separation bubble pressure level (computation versus experiment) and 5) separation bubble wall heat transfer (computation versus experiment).

Statistics for these uncertainty measures were collected for each experimental case and evaluated for bias, variance and both 90% and

95% confidence intervals, with the results reported for the attached cases and for the separated cases separately.

Significant levels of bias and variance were seen in the simulations for these cases emphasizing a high level of uncertainty in the turbulence modeling for hypersonic SWTBLIs. Discussed was the possibility of *calibrating* the CFD analysis procedure for bias effects so as to provide a useful analytic technique for design. However, the large variance present in the uncertainty measures implies that the bias is highly inconsistent precluding reliable calibration.

Both the SST and K-ω performed similarly, but demonstrated confidence limit bounds that reach 50%. The SST model and the K-ω models tend to exhibit an overshoot in wall heating past reattachment for separated cases, with a tendency to underpredict the separation extent. The separation bubble pressure and wall heat transfer levels for separated regions were underpredicted by ≈25–40%. The Spalart–Allmaras model proved to systematically resist separation.

Where the turbulent boundary layer was thin relative to a long shock generator length ($L_g/\delta_0 \approx 1000$) the CFD wall heating overshoot proved most severe, whereas a boundary layer thick relative to a short shock generator length ($L_g/\delta_0 \approx 110$) appeared to enable the shock generator trailing-edge expansion fan to mitigate the severity of the interaction in the vicinity of reattachment and yields more accurate simulations.

An implementation sensitivity study provides a basis for positive outlook, however, as two approaches examined, that of an improved wall boundary condition treatment and a modified compressibility correction appear to provide improvement in the simulation of separated flows. Furthermore, a hybrid CFD-correlation approach was shown to yield improved peak heating estimates in the vicinity of SWTBLIs.

None of the experiments considered, although hypersonic, exhibited real gas or dissociation effects. A literature search concluded that no such SWTBLI experiments exist for both high-enthalpy and turbulent conditions likely to be encountered in flight. Simulations of a "nominal-trajectory flight case" provided a basis for sensitivity studies of real gas effects under potential flight conditions. Such effects were found to occur in the simulations, leading to an increase in peak heating of 20% and reduction in separation extent. This in spite of less than 1% dissociation of molecular oxygen into atomic oxygen for the conditions simulated.

The high level of uncertainty observed in these simulations is believed to be free of correctable errors and is primarily due to turbulence model deficiencies. The impact this may have on scramjet development suggests a compelling need for high-enthalpy, real gas experiments for impinging SWTBLI so as to complete the assessment of the sensitivity of the current methods to flows where dissociation occurs and to reduce the current high levels of turbulence modeling uncertainty through modeling improvements.

Appendix A: Turbulence Model Equations

I. Spalart–Allmaras One-Equation Model

The Spalart–Allmaras one-equation turbulence model solves for an eddy viscosity-like variable, $\hat{\nu}$, from which the eddy viscosity is then algebraically determined. The standard Spalart–Allmaras model inadequately replicates the compressible log-law-of-wall region, so modifications by Catris and Aupoix must be applied. The Catris and Aupoix modified form of the Spalart–Allmaras model is given by

$$(\partial\rho\hat{\nu}/\partial t) + (\partial\rho u_j\hat{\nu}/\partial x_j) = c_{b1}S_{\text{sa}}\rho\hat{\nu} - c_{w1}f_w\rho(\hat{\nu}/d)^2 + \sigma^{-1}\partial/\partial x_j[(\mu+\rho\hat{\nu})(\partial\hat{\nu}/\partial x_j)] + (c_{b2}\sigma^{-1})\rho(\partial\hat{\nu}/\partial x_i)(\partial\hat{\nu}/\partial x_i) \tag{A1}$$

with the eddy viscosity then obtained by

$$\mu_t = \rho\hat{\nu}f_{v1} \tag{A2}$$

Where

$$f_{v1} = \hat{\nu}^3/(\hat{\nu}^3 + \nu c_{v1}), \qquad f_{v2} = 1 - \hat{\nu}/(\nu + f_{v1}\hat{\nu}),$$
$$\hat{S} = \Omega + \hat{\nu}f_{v2}/(\kappa d)^2, \qquad r = \min(\hat{\nu}/(\hat{S}(\kappa d)^2)), 10),$$
$$g = r + c_{w2}(r^6 - r), \qquad f_w = g[(1+c_{w3}^6)/(g^6 + c_{w3}^6)]^{1/6},$$
$$c_{w1} = (c_{b1}/\kappa)^2 + (1+c_{b1})/\sigma \tag{A3}$$

$$c_{b1} = 0.1355; \qquad c_{b2} = 0.622; \qquad c_{v1} = 7.1; \qquad c_{w2} = 0.3;$$
$$c_{w3} = 2; \qquad \sigma = 2/3 \tag{A4}$$

Boundary conditions are

$$\hat{\nu} = 0 \quad \text{at wall}, \qquad \hat{\nu} = 3\nu_\infty \quad \text{at } \infty \tag{A5}$$

II. Menter SST/K-ω Two-Equation Turbulence Model

The shear stress transport model was introduced by Menter [5], incorporating concepts of Coakley and combining desirable compressible boundary-layer properties of the Wilcox 1988 K-ω model with desirable free shear layer behavior of Launder's K-ϵ model. The blending of the Wilcox K-ω model for inner boundary layer with a K-ω transformed form of the K-ϵ equations for the outer boundary layer and free shear layer introduces two sets of constants along with a blending function, F_1. The transformation of the K-ϵ equation set into the "outer" K-ω form, also led to the extra "cross-diffusion," $(\partial k/\partial x_j)(\partial\omega/\partial x_j)$, transport term in the ω equation and which is valid only for the outer boundary layer and free shear viscous regions. F_1 is designed to be ≈1 close to the wall and through the log-layer of the boundary layer, then reducing to ≈0 in the freestream and for free shear viscous shear flows. The resulting SST equation set is

$$(\partial\rho K/\partial t) + (\partial\rho u_j K/\partial x_j) = \hat{P}_K - \beta^*\rho\omega K + \partial/\partial x_j[(\mu+\sigma^*\mu_t)(\partial K/\partial x_j)] \tag{A6}$$

$$(\partial\rho\omega/\partial t) + (\partial\rho u_j\omega/\partial x_j) = P_\omega - \beta\rho\omega^2 + \partial/\partial x_j[(\mu+\sigma_\omega\mu_t)(\partial\omega/\partial x_j)] + 2(1-F_1)(\rho\sigma_{\omega2}/\omega)[(\partial K/\partial x_j)(\rho\omega/\partial x_j)] \tag{A7}$$

The production terms are

$$P_K = \tau_{ij}\partial u_i/\partial x_j = \mu_t\hat{S}^2 - (2/3)\rho K(\partial u_i/\partial x_j)\delta_{ij} \tag{A8}$$

$$P_\omega = \gamma\rho P_K/\mu_t \tag{A9}$$

The traceless-strain tensor "magnitude," $\hat{S}$, is

$$\hat{S}^2 = 2\hat{S}_{ij}\hat{S}_{ij} \tag{A10}$$

$$\hat{S}_{ij} = (\partial u_i/\partial x_j + \partial u_j/\partial x_i)/2 - (\partial u_l/\partial x_l)\delta_{ij}/3 \tag{A11}$$

A production limiter is applied to P_K, for the TKE equation only, such that $\hat{P}_K \leftarrow \min(P_K, 10\beta^*\rho\omega K)$.

The eddy viscosity incorporates the length-scale modification of Vuong and Coakley [67]:

$$\mu_t = \rho\min(\kappa d\sqrt{a_1 K}, K/\max(\omega, F_2\hat{S}/a_1)) \tag{A12}$$

Where, $\beta^* = 0.09$, $\kappa = 0.41$, $a_1 = 0.31$, and the constants for γ, β_ω, σ_ω, and σ^* used in the equations are formed by interpolation between the two sets of constants by

$$\Phi = F_1\Phi_1 + (1-F_1)\Phi_2 \tag{A13}$$

The two SST constant sets (inner, 1; outer, 2) are

$$\gamma_1 = 0.5532, \quad \beta_{\omega 1} = 0.0750, \quad \sigma_{\omega 1} = 0.500,$$
$$\gamma_2 = 0.4404, \quad \beta_{\omega 2} = 0.0828, \quad \sigma_{\omega 2} = 0.856,$$
$$\sigma_1^* = 0.85, \quad \sigma_2^* = 1.00$$

The blending function, F_1, varies from 1.0 for the "inner" boundary layer, to 0.0 for the outer boundary layer, freestream and free shear layer regions and is constructed by

$$F_1 = \tanh(arg_1^4),$$
$$\text{where } CD_{K\omega} = \max((2\rho\sigma_{\omega 2}[(\partial K/\partial x_j)(\partial\omega/\partial x_j)]/\omega), 10^{-10})$$
$$arg_1 = \min[\max(\sqrt{k}/\beta^*\omega d, 500\mu/\rho\omega d^2), 4\rho\sigma_{\omega 2}K/CD_{K\omega}d^2] \tag{A14}$$

Note, d is the wall-normal distance of the cell to the nearest wall. And, the constitutive blending function, F_2 is constructed by

$$F_2 = \tanh(arg_2^2),$$
$$\text{where } arg_2 = \max(2\sqrt{K}/\beta^*\omega d, 500\mu/\rho\omega d^2) \tag{A15}$$

Variations on SST boundary conditions and other treatments are described in Appendix B.

III. Wilcox-2006 K-ω Two-Equation Turbulence Model

The K-ω model, as developed by Wilcox [6,7] by design, exhibits better replication of compressible log-law-of-the-wall behavior than the earlier K-ϵ model, and has proven to be well-suited for compressible flows. The competing K-ϵ model requires considerable correction for compressible turbulent boundary layers. The latest formulation [7] incorporates the "cross-diffusion" term, $(\partial k/\partial x_j)(\partial\omega/\partial x_j)$, of Menter, but without requiring blending functions or the wall-normal distance. An aversion to the wall-normal distance can be traced to a perception that it is awkward and costly to compute accurately, but it is often used in well-established turbulence correlations. Similar to Cebeci and Smith's development of their algebraic model [68], Wilcox has spent considerable effort to incorporate various physics effects into this model, including roughness, blowing, compressibility corrections, etc.

The Wilcox-2006 K-ω equation set is

$$(\partial\rho K/\partial t) + (\partial\rho u_j K/\partial x_j) = \hat{P}_K - \beta_K\rho\omega K + \partial/\partial x_j[(\mu + \sigma_K\rho K/\omega)(\partial K/\partial x_j)] \tag{A16}$$

$$(\partial\rho\omega/\partial t) + (\partial\rho u_j\omega/\partial x_j) = P_\omega - \beta\rho\omega^2 + \partial/\partial x_j[(\mu + \sigma_\omega\rho K/\omega)(\partial\omega/\partial x_j)] + (\rho\sigma_d/\omega)[(\partial K/\partial x_j)(\rho\omega/\partial x_j)] \tag{A17}$$

The production terms are

$$P_K = \tau_{ij}\partial u_i/\partial x_j = \mu_t\hat{S}^2 - (2/3)\rho K(\partial u_i/\partial x_j)\delta_{ij} \tag{A18}$$

$$P_\omega = \alpha\omega P_K/K \tag{A19}$$

As the DPLR primary focus is hypersonic flows with strong shocks, the SST production limiter is also applied for the Wilcox K-ω model, for the TKE equation only, such that $\hat{P}_K \leftarrow \min(P_K, 10\beta_K\rho\omega K)$.

The eddy viscosity incorporates the length-scale modification of Vuong and Coakley [67]:

$$\mu_t = \rho\min(\kappa d\sqrt{a_1 K}, K/\max(\omega, C_{\lim}\hat{S}/\sqrt{\beta_K})) \tag{A20}$$

The K-ω 2006 constant set is

$$\alpha = 0.52, \quad C_{\lim} = 7/8, \quad \sigma_K = 0.60, \quad \sigma_\omega = 0.50,$$
$$\beta_K = 0.09, \quad \beta_\omega = \beta_0 \cdot f_\beta, \quad \beta_0 = 0.0708$$
$$\sigma_d = 1/8, \quad \text{for } (\partial K/\partial x_j)(\partial\omega/\partial x_j) < 0, \quad =0, \quad \text{otherwise}$$

where

$$f_\beta = (1 + 85\chi_\omega)/(1 + 100\chi_\omega); \qquad \chi_\omega = |\Omega_{ij}\Omega_{jk}\check{\check{S}}_{ki}|/(\beta_K\omega)^3$$
$$\check{\check{S}}_{ki} = S_{ki} - (\partial u_l/\partial x_l)\delta_{ki}/2; \qquad \Omega_{ij} = (\partial u_i/\partial x_j - \partial u_j/\partial u_i)/2 \tag{A21}$$

Variations on boundary conditions and other treatments are similar to the SST model, see Appendix B.

For all turbulence models in the current simulations, the eddy diffusivities for turbulent heat transfer and for turbulent mass transfer are found from the turbulent eddy viscosity using a constant turbulent Prandtl number ($Pr_t \approx 0.9$) and turbulent Schmidt number ($Sc_t \approx 0.7$), respectively, in the mean flow equations.

Appendix B: SST Turbulence Model Implementation Option-Grid Sensitivity

To facilitate examining turbulence model "error," a wide variety of implementation options of interest were incorporated into DPLR v4.01.01, selecting amongst them by command-line option. We verified results from the modified code without command-line options (selecting the DPLR default) and compared with the unmodified DPLR v4.01.1 results to ensure that new code errors had not been introduced. These implementation options were first applied to hypersonic flat plate flows and the results are examined to determine which of these modeling choices introduce avoidable modeling "errors," before applying the models to the impinging SWTBLI cases.

I. Implementation Option Discussion and Definitions

The turbulence model implementation options specifically incorporated for this study, then, were:

A. *Turbulent Production Terms*

Many hypersonic applications involve blunt bodies with curved bow shocks. The exact or "strain-based" turbulence production term has a known tendency to overpredict turbulent production for flow streamtubes passing through a strong curved bow shock, and a further known tendency to overpredict turbulent production along stagnating streamlines. The "vorticity-based" production formulation arose out of those concerns, because within an attached 2D boundary layer, at least, there will be little difference between a "vorticity-based" and a "strain-based" formulation. Note that the "strain-based" formulation actually makes use of the traceless-strain magnitude, and for all production formulations the divergence term is subtracted for compressible flows (see the preceding equation). To correct for stagnation overproduction, Kato and Launder [69] suggested their mixed vorticity/strain-based form. We propose an alternative hybrid vorticity/strain form where the vorticity formulation is used in freestream and laminar regions (to facilitate numerical transition) and the strain based formulation is used within turbulent viscous regions, whether wall bounded or free shear. These turbulent production options [for the first term of Eq. (A8)] are as follows:

iProdK = 0: "vorticity-based" production where $P_{K,0} \approx \mu_t\Omega^2$.

iProdK = 1: "strain-based" production, $P_{K,1} \approx \mu_t\hat{S}^2$.

iProdK = 2: "Kato–Launder" mixed vorticity stress, $P_{K,2} \approx \mu_t\Omega\hat{S}$.

iProdK = 3: hybrid vorticity/stress production form, where $P_{K,3} \approx \mu_t((1 - F_p)\Omega^2 + F_p\hat{S}^2)$.

In the hybrid vorticity/stress production form, a logic switch is designed to distinguish turbulent viscous regions whether wall bounded or free shear (where $F_p \approx 1$) from the freestream region (i.e., through a bow shock, etc., where $F_p \approx 0$): $F_p \equiv [F_1 + (1 - F_1)/(1 + \exp(12 - (K/K_\infty) - (\omega/\omega_\infty)))]$.

Depending on which option (0–3) is chosen, the turbulent production term Eq. (A8) becomes

$$P_K = P_{K,0-3} - (2/3)\rho K(\partial u_i/\partial x_j)\delta_{ij} \tag{B1}$$

B. Compressibility Correction Terms

For compressible free shear layers, the growth rate is reduced due to high levels of turbulent Mach number, $M_t \equiv \sqrt{2K/a^2}$. Wilcox reports corrections to the K-ω constants for β_K and β_ω to reduce the eddy viscosity in compressible free shear layers as derived by several similar theories. Details are found in Wilcox [7], but here the free shear layer compressibility correction options are as follows:

iCompC $= -1$: do not apply.
iCompC $= 0$: default model behavior.
iCompC $= 1$: Sarkar correction.
iCompC $= 2$: Zeman correction.
iCompC $= 3$: Wilcox correction.

Experience with these free shear layer compressibility corrections are, however, that they are unnecessary for attached wall boundary layers. If they are applied due to the presence in a supersonic/hypersonic application of both wall and free shear layers, it is found that the resulting reduction of eddy viscosity from these corrections lead to invalid shear stress and heating solutions. By applying a simple correction [12] to the turbulent Mach number where now $\hat{M}_t^2 = (1 - F_1) \cdot M_t^2$, with F_1 being the SST blending function, which is $\approx$1 within an attached wall boundary layer, but $\approx$0 outside the wall boundary layer, is used in the compressibility correction in place of M_t, the correct behavior for *both* free shear layers and wall boundary layer would result. The corresponding options with $\hat{M}_t$ applied become the following:

iCompC $= 4$: Sarkar/Brown.
iCompC $= 5$: Zeman/Brown.
iCompC $= 6$: Wilcox/Brown.

To be determined, in this study, is which form is best applied to a separated wall boundary layer, if at all.

C. Convective Term Order

iKOrder $= 2$: use second-order convective term in Turb model PDE.

iKOrder $=$ otherwise: use first-order convective term in Turb model PDE.

D. Wall Viscous Sublayer And Log-Layer Analytical Equations

In the near wall viscous sublayer of a turbulent boundary layer, the convective and streamwise diffusion terms of the K-ω equations become negligible, which results in analytical solutions for both K and ω. Additionally, an analytical form for the ω term can be derived for the equilibrium log-wall-layer, traceable to Vuong and Coakley [67]. Use of these analytical relations can assure that the ω term does not drop too low due to numerical integration and grid-related errors. Two ways to implement this analytical "assistance" can be employed. The first is "explicit" in that after solving the model equations simply overwrite ω should it drop below the analytical-derived value. The second approach, used by this author, employs the analytical expressions in the implicit setup of the diffusion terms, e.g., if ω at a neighbor point is below the analytical value, then the analytical value is substituted. This cures a problem observed with finely spaced grids within the viscous sublayer, where the ω value is dropping from "near" infinity at the wall, an undershoot develops with increasing normal wall distance, leading to the eddy viscosity rising too rapidly for the near wall, with attendant high heating for fine grids. By performing this implicitly, the near wall ω is forced nearly to the analytical expression without oscillation associated with the explicit approach. Note that near wall errors in eddy viscosity can have a disproportionate effect on wall heating, as the near wall processes dominate heating. The options become (wall values for β_ω and β^* are used) the following:

iOmegaAn $= -1$: do not apply.
iOmegaAn $= 0$: default model behavior.
iOmegaAn $= 1$: $\omega = 6\mu/(\beta_\omega \rho y^2)$.
iOmegaAn $= 2$: $\omega = (6\mu/(\beta_\omega \rho y^2)) + (\sqrt{K}/((\beta^*)^{0.25}\kappa y))$.

E. Turbulence Model Wall Boundary Condition Terms

The analytical value for ω tends to ∞ as the wall is approached, so a large value is often suggested for use in wall boundary conditions. Several such ω-equation wall boundary condition options appear in the literature:

iWallBC0 $= 0$: $\omega_w = 40,000\mu/(\rho y_1^2)$, DPLR default.
iWallBC0 $= 1$: $\omega_w = 3200\mu/(\rho y_1^2)$, from Menter.
iWallBC0 $= 2$: $\omega_w = 40,000\Omega_w$, based on Wilcox for smooth wall, where y_1 is the "cell thickness" of the first finite volume cell off the wall. The wall boundary condition for the K-equation is simply $K = 0$. These iWallBC0 option choices are relevant only if the next option is iWallBC1 $= -1$ or 0.

We shall see that little difference appears in these iWallBC0 "wall boundary condition" choices, whereas certain iWallBC1 "wall treatment" choices seem advantageous.

F. Wall Viscous Layer "Treatment" Terms

In place of applying a wall boundary condition, analytical correlations can be applied for the near wall points directly within the implicit process. Rather than solve the turbulence model PDE equations within these innermost cells, the matrix term diagonal is set to one, and off-diagonal terms set to zero. This approach precludes setting an actual wall boundary condition. This option can be activated for the K and ω equations separately. The options are as follows:

iWallBC1 $= -1$: do not apply, MUST choose iWallBC0 > 1.
iWallBC1 $= 0$: use default behavior for DPLR and turbulent model.
iWallBC1 $= 1$: use analytical expression for ω equation at first point off wall.
iWallBC1 $= 2$: use analytical expression for both the K and ω equation at first point off wall.
iWallBC1 > 2: use analytical expressions for up to $y+ = 6$, and up to npts $= 7$ off the wall, according to relations described.

Note that the K equation can be analyzed for its viscous sublayer behavior similar to the analytical analysis of the near wall behavior of the ω equation, with a result of $K \approx a_k y^n$, where n lies between 3 and 4 depending on whether it is the SST or Wilcox K-ω model. The constant a_k is not determined by the near wall analysis, however, because the value of K and its first-through-$(n-1)$ derivatives are zero at the wall, and we interpret this indeterminate result to mean the near wall behavior of K may be ill-conditioned. It appears this may be the source of observed grid-dependency of the K-ω models, a complication later demonstrated to be repairable. The actual physical variation of K in the viscous sublayer is believed to be $K \approx y^2$, but it is the model equations that establish grid-dependency.

G. Catris and Aupoix Modification

Analysis of the several PDE-based turbulence model equations for behavior for the compressible log-law-wall region revealed that certain viscous diffusion modification resulted in better performance, particularly for the K-ϵ and Spalart–Allmaras forms. A minor correction suggested for K-ω is not commonly used because the K-ω compressible log-law behavior is nearly correct:

iCatris ≤ -1: do not use Catris and Aupoix correction.
iCatris $= 0$: default model behavior.
iCatris ≥ 1: use Catris and Aupoix correction.

H. Eddy Viscosity "CLIM" term

A limiter is introduced on the eddy viscosity term, in both the Menter SST and Wilcox forms of the K-ω equation. Wilcox has fixed

the coefficient for the limiter at 7/8, whereas Menter's form implies a value of 1. Some authors have modified this for SWTBLI to get better agreement with separation length. Here the SST options are as follows:

iCLIM = 0: use default model behavior.

iCLIM = 2: use clim = 0.9 in eddy viscosity expression.

iCLIM = otherwise: use clim = 1.0.

These options affect only the K-ω equations, and not the mean Navier–Stokes.

II. SST Implementation Options: Mach 10 Flat Plate Sensitivity Study

A. *"Nominal" $M_\infty = 10$, Cold Wall, 2D Flat Plate Boundary Layer*

The Mach 10 cold wall Flat Plate boundary layer is used to examine the impact of specific SST implementation options on heating simulations of a turbulent hypersonic cold wall flat plate boundary layer. The intent is not to determine which turbulence model or which option is the *best* to implement, because here we examine only one flow, and a general purpose turbulence model needs evaluated against a wide range of flows. Rather it is a process of elimination, to determine whether any of these options should not be used.

The Mach 10 case is computed with 10-m-long 2D Flat Plate grids, of both a medium $128 \times 3 \times 128$ and a fine $256 \times 3 \times 256$ grid resolution. Most of the solutions were obtained on the medium grid, as little change occurred in going to fine resolution, and the purpose was implementation sensitivity studies, rather than validation. The freestream conditions were Mach = 10, $U = 3472.47$ m/s, $2.6587 \cdot 10^{-2}$ Kg/m^3, $T_\infty = 1900$ K, $T_0 = 6000$ K, $T_w = 300$ K giving $ReU = 5 \cdot 10^6$. All computations were with *DPLR3D*, running in full 3D mode even for this 2D case, as this mode is most used for NASA's mission study and support functions.

B. *SST Free Shear Compressibility Correction Sensitivity*

Supersonic and hypersonic free shear layer flows grow at a slower rate than for incompressible. Three forms of free shear layer compressibility corrections have been proposed for SST and K-ω two-equation models. These are the Sarkar, Zeman, and Wilcox compressibility corrections all of which seek to account for the same effect. These act by reducing the turbulence levels and associated eddy viscosity, an effect that should not be applied to viscous wall layers. For more complex simulations which involve both types of flows, the decision whether to use the standard forms of these corrections is complicated, because the improvement in free shear layer performance can lead to degraded performance for the attached wall layers. Note that the Wilcox compressibility correction will "turn off" for a supersonic boundary layer up to about Mach 5, but for higher Mach numbers all of these corrections tend to erroneously lower eddy viscosity in hypersonic turbulent boundary layers. Significantly lower values of computed wall heat transfer and shear stress result.

It is clearly desirable to have the free shear layer corrections controlled by a computed logical switch that detects whether the region of flow is a free shear layer or viscous wall. Brown [12] showed that using the F_1 blending function already available in the SST model could act as such a computed logical switch to control as to which type of region the free shear layer compressibility correction is applied.

In Figs. B1 and B2 are shown the effect on a Mach 10 hypersonic cold wall boundary layer of these free shear layer compressibility corrections implemented into the SST turbulence model. Figure B1 compares the wall heating for the three free shear layer compressibility correction against the standard SST demonstrating the large dropoff in wall heat transfer associated with these corrections for a hypersonic viscous wall layer. In contrast, Fig. B2 shows that by incorporating the modification suggested by Brown, the use of any of these three free shear layer compressibility correction no longer incorrectly reduces hypersonic turbulent boundary-layer heat transfer. Not addressed here is the effectiveness of the free shear layer compressibility corrections for supersonic and hypersonic free shear layers, as that is not a topic of this paper. Rather, the modified compressibility corrections becomes for a free shear layer as effective as the original form, the discussion of Wilcox [7] regarding the unmodified forms should be referred to. The modification, given by Brown [12], is simply to use in the correction the F_1 modified form for the turbulent Mach number, e.g., $\hat{M}_t^2 = (1. - F_1)2 \cdot (K/a^2)$. The term $(1 - F_1)$ will be zero for the inner portion of a wall boundary layer, where the free shear layer compressibility corrections should not be applied, and will equal one for free shear layer flows, where the free shear layer compressibility correction should be applied. We examine in the paper's main body, the use of these corrections for separated SWTBLI.

C. *Turbulence Model y_1^+ Grid Sensitivity*

Figure B3 shows y_1^+ grid sensitivity for the turbulence models; the Baldwin–Lomax, the Spalart–Allmaras, and the SST turbulence models. The location plotted is at the end of the flat plate, where $Re_x \approx 5 \cdot 10^6$. The K-ω model has behavior similar to SST. Four similar grids are used for all models, the difference being the spacing of the first grid point varies from $y_1^+ = 0.05$ to 1.5. Only the Spalart–

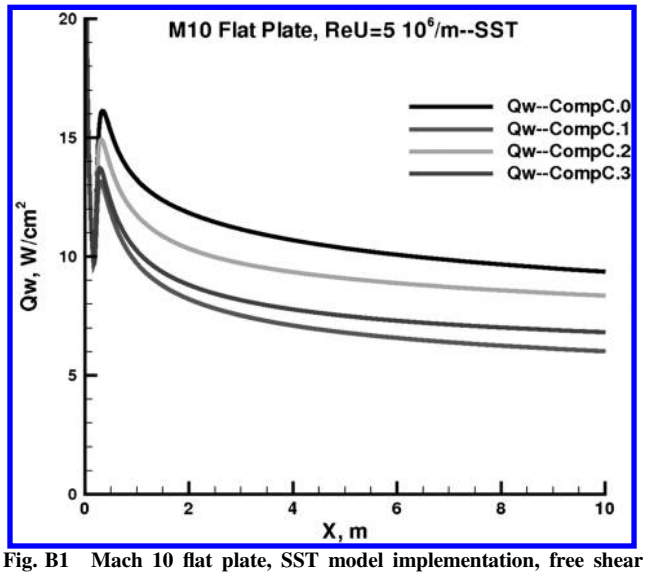

Fig. B1 Mach 10 flat plate, SST model implementation, free shear compressibility corrections. Cold wall, $T_w/T_0 = 1/3$.

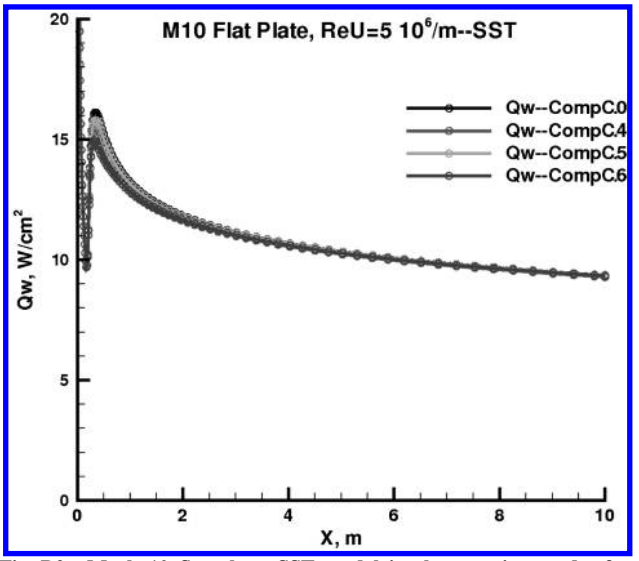

Fig. B2 Mach 10 flat plate, SST model implementation study, free shear compressibility corrections, F_1-modified-Sarkar, Zeman, and Wilcox. Cold wall, $T_w/T_0 = 1/3$.

Allmaras exhibits complete grid insensitivity to y_1^+ spacing, but the heating result is considerably higher than the Baldwin–Lomax result, usually considered the most accurate for "acreage" heating. The Baldwin–Lomax model has a slight y_1^+ grid sensitivity, being within 1–2% over this range. Both the SST and the K-ω models exhibit considerably greater y_1^+ grid sensitivity requiring that the initial $y_1^+ < 0.3$ for the solution to be within 1–2% of the final converged solution. It is for the $y_1^+ \approx 0.5$ grid that the SST model gives similar wall heating as the Baldwin–Lomax, however, with the SST model tending to be about 5% higher in wall heating than Baldwin–Lomax at the tightest y_1^+ grid spacing.

D. SST Wall Boundary Condition/Treatment-Grid Sensitivity

Fairly tight grid spacing with $y_1^+ < 0.3$ is recommended for the SST model by most code implementors due to the y_1^+ grid sensitivity shown in Fig. B3 for the standard SST model. The numerous variations in wall boundary condition treatment for the SST model and enumerated as options iWallBC0 and iWallBC1 were explored. For nearly all combinations of these wall boundary condition options, considerable grid sensitivity is seen. Most of these wall boundary condition options yield similar behavior to the standard SST performance plotted in Fig. B3 and thus not plotted.

However, also shown in Fig. B3 are the iWallBC1.6 option results in that it led to a significant improvement in y_1^+ grid sensitivity. For this option, the value of ω is implicitly set for those cells near the wall according to the near wall ω analytical equation, up to $y^+ = 6$, but otherwise proceeding with the PDE solution process. As a consequence, no "wall" value is used for this option, and the oscillatory behavior induced by an explicit reset of near wall ω is avoided. Cells located further from the wall are solved for using the standard K-ω PDE set. Only for initial grid points larger than y^+ of 1 is grid sensitivity of heat transfer to grid spacing seen. Some further improvement could be obtained at larger y_1^+ by detailed changes in the analytical form of the ω sublayer-buffer equation, which is being actively pursued.

E. SST Turbulent Production Term Sensitivity

The vorticity-based "Prodk.0" option was preferentially implemented into DPLR originally, not because it is slightly easier, but rather because in going through a bow-shock of reentry vehicles, false production of turbulent kinetic energy due to numerical noise is avoided. The stress-based "Prodk.1" is considered to be the exact production term. However, for streamlines passing through a strong bow-shock, this exact production term will induce nonphysical levels

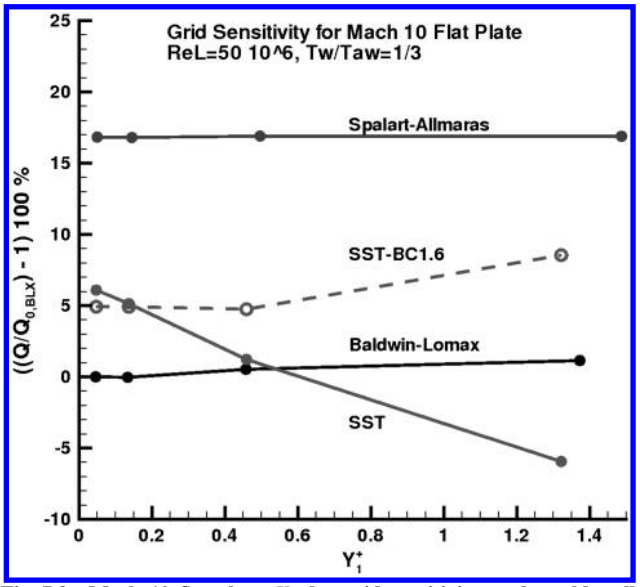

Fig. B3 Mach 10 flat plate, Y plus grid sensitivity study, cold wall, $T_w/T_0 = 1/3$.

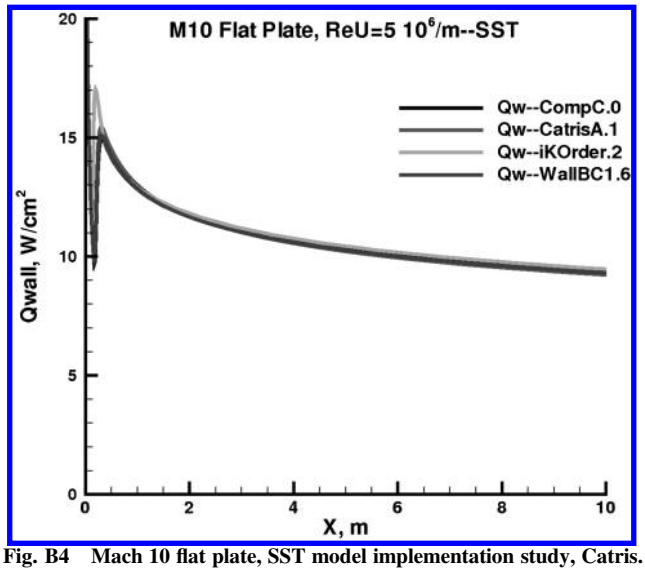

Fig. B4 Mach 10 flat plate, SST model implementation study, Catris. Cold wall, $T_w/T_0 = 1/3$.

of turbulence. The other turbulent production options are designed as intermediate between these two choices. In particular, the "Prodk.2" option is by Launder, intended to improve solutions in the vicinity of a stagnation point for the K-ϵ model. The "Prodk.3" option is controlled by a logical switch, F_p designed to activate the stress-based option for turbulent viscous regions, regardless of whether free shear layer or viscous wall, while retaining the vorticity-based production option for low turbulence region such as the freestream or streamlines passing through a bow-shock. For the present simulations for the cold wall turbulent boundary layer all turbulent production options considered gave virtually identical solutions, hence no figure is given.

F. Additional SST Implementation Option Sensitivity

Finally, Fig. B4 shows characteristic comparisons of wall heating for this Mach 10 case for several additional SST implementation options. In this figure, the compressibility corrections of Catris and Aupoix are applied to the SST equations (CatrisA.1) and exhibit minimal effect relative to the standard (CompC.0 option) SST solutions, as expected. Typically, we do not run SST solutions with the Catris option for SST, as the Catris modification is intended to improve compressible turbulent boundary-layer solutions for the Spalart–Allmaras and K-ϵ models. Additionally, the use of a second-order convective term in the K-ω equation as opposed to our usual use of first-order seems to raise heat transfer levels slightly. Note, only the convective term is treated first order in our current SST implementation, all other terms are second order. Also, the grid-insensitive "WallBC1.6" option gives essentially identical solution as does the standard or "CompC.0" option. The agreement is because the grid used has the tightest $y_1^+ = 0.05$ grid spacing.

To avoid ambiguity, the DPLR-*standard* implementation is used for all solutions of this paper except where noted and entails the default choice of vorticity-based production, no compressibility correction, first-order convective terms, and the iWallBC0 = 0, iWallBC1 = 0, and iOmegaAn = 2 model implementation options.

Acknowledgments

This research was sponsored by NASA's Fundamental Aeronautics Program: Hypersonics project. The interest, leadership, and support of Deepak Bose (Associate Project Investigator, Hypersonics) are gratefully acknowledged. Technical discussions on turbulent physics and uncertainty with Joseph G. Marvin and Nagi N. Mansour were most helpful. The professional skills and kind efforts of the NASA Ames Research Center library staff, particularly those of Kathy Ponce and Dan Pappas, are much appreciated.

References

[1] Billig, F., "Research on Supersonic Combustion," *Journal of Propulsion and Power*, Vol. 9, No. 4, July–Aug. 1993, pp. 499–514. doi:10.2514/3.23652

[2] Bose, D., Brown, J. L., Prabhu, D. K., Gnoffo, P. A., Johnston, C. O., and Hollis, B., "Uncertainty Assessment of Hypersonic Aerothermodynamics Prediction Capability," AIAA Paper 2011-3141, Honolulu, HI, 27–30 June 2011.

[3] Gnoffo, P. A., Berry, S. A., and Van Norman, J. W., "Uncertainty Assessments in Simulations of 2D and Axisymmetric Hypersonic Shock Wave-Turbulent Boundary Layer Interactions at Compression Corners," AIAA Paper 2011-3142, Honolulu, HI, 27–30 June 2011.

[4] Wright, M. J., Candler, G. V., and Bose, D., "Data-Parallel Line Relaxation Method for the Navier–Stokes Equations," *AIAA Journal*, Vol. 36, No. 9, 1998, pp. 1603–1609. doi:10.2514/2.586

[5] Menter, F. R., "Two-Equation Eddy Viscosity Turbulence Models for Engineering Applications," *AIAA Journal*, Vol. 32, No. 8, Aug. 1994, pp. 1598–1605. doi:10.2514/3.12149

[6] Wilcox, D. C., "Reassessment of the Scale-Determining Equation for Advanced Turbulence Models," *AIAA Journal*, Vol. 26, No. 11, Nov. 1988, pp. 1299–1310. doi:10.2514/3.10041

[7] Wilcox, D. C., *Turbulence Modeling for CFD*, 3rd ed., DCW, La Canada, CA, 2006.

[8] Spalart, P. R., and Allmaras, S. R., "A One-Equation Turbulence Model for Aerodynamic Flows," *Recherche Aerospatiale*, No. 1, 1994, pp. 5–21.

[9] Catris, S., and Aupoix, B., "Density Corrections for Turbulence Models," *Aerospace Science and Technology*, Vol. 4, No. 1, 2000, pp. 1–11. doi:10.1016/S1270-9638(00)00112-7

[10] Sarkar, S., Erlebacher, G., Hussain, M. Y., and Kreiss, H. O., "The Analysis and Modelling of Dilatational Terms in Compressible Turbulence," *Journal of Fluid Mechanics*, Vol. 227, 1991, pp 473–493. doi:10.1017/S0022112091000204

[11] Zeman, O., "Dilatation Dissipation: The Concept and Application in Modeling Compressible Mixing Layers," *Physics of Fluids A*, Vol. 2, No. 2, 1990, pp 178–188. doi:10.1063/1.857767

[12] Brown, J. L., "Turbulence Model Validation for Hypersonic Flows," Eighth AIAA/ASME Joint Thermophysics and Heat Transfer Conference, AIAA Paper 2002-3308, St. Louis, MO, 24–26 June 2002.

[13] Ames Research Staff, "Equations, Tables, and Charts for Compressible Flow," NACA Rept. 1135, 1953.

[14] Chapman, D. R., Kuehn, D. M., and Larson, H. K., "Investigation of Separated Flows in Supersonic and Subsonic Streams with Emphasis on the Effect of Transition," NACA Rept. 1356, 1958.

[15] Erdos, J., and Pallone, A., "Shock-Boundary Layer Interaction and Flow Separation," *Proceedings of the Heat Transfer and Fluid Mechanics Institute*, edited by F. E. Ehlers, J. J. Kauzlarich, C. A. Sleicher, and R. E. Street, Stanford Univ. Press, Stanford, CA, 13–15 June 1962.

[16] Delery, J., and Marvin, J. G., "Shock-Wave Boundary Layer Interactions," edited by E. Reshotko, NATO, AGARDograph AG-280, 1986.

[17] Kussoy, M. I., Brown, J. D., Brown, J. L., Lockman, W. K., and Horstman, C. C., "Fluctuations and Massive Separation in Three-Dimensional Shock-Wave/Boundary Layer Interactions," *Proceedings of the International Symposium on Transport Phenomena in Turbulent Flows*, 2nd ed., Univ. of Tokyo, Tokyo, 1988, pp. 875–887.

[18] Brown, J. L., Kussoy, M. I., and Coakley, T. J., "Turbulent Properties of Axisymmetric Shock-Wave/Boundary-Layer Interaction Flows," *Turbulent Shear-Layer/Shock-Wave Interactions*, edited by J. Delery, Springer–Verlag, Berlin, 1986, pp. 137–148.

[19] Thompson, M. J., "A Note on the Calculation of Oblique Shock-Wave Characteristics," *Journal of Aeronautical Sciences*, Vol. 17, No. 11, 1950, p. 744.

[20] Wolf, T., "Comment on 'Approximate Formulation of Weak Oblique Shock Wave Angle'," *AIAA Journal*, Vol. 31, No. 7, 1993, p. 1363. doi:10.2514/3.49078

[21] Hopkins, E. J., and Inouye, M., "An Evaluation of Theories for Predicting Turbulent Skin Friction and Heat Transfer on Flat Plates at Supersonic and Hypersonic Mach Numbers," *AIAA Journal*, Vol. 9, No. 6, June 1971, pp. 993–1003. doi:10.2514/3.6323

[22] Rubesin, M. W., and Inouye, M., "Forced Convection, External Flows," *Handbook of Heat Transfer*, 1st ed., edited by W. M. Rohsenow and J. P. Hartnett, McGraw–Hill, New York, 1973, pp. 8–148.

[23] Van Driest, E. R., "The Problem of Aerodynamic Heating," *Aeronautical Engineering Review*, Vol. 15, No. 10, Oct. 1956, pp. 26–41.

[24] Shoenherr, K. E., "Resistance of Flat Surfaces Moving Through a Fluid," *Transactions: The Society of Naval Architects and Marine Engineering*, Vol. 40, 1932, pp. 279–313.

[25] Coakley, T. J., "Data and Empirical Correlations for Simple Flows," *GWP 18 Technology Exchange Meeting*, NASA Ames Research Center, Moffett Field, CA, 31 Oct.–1 Nov. 1991.

[26] White, F., M., *Viscous Fluid Flow*, 1st ed., McGraw–Hill, New York, 1974.

[27] Lockman, W. K., Lawrence, S. L., and Cleary, J. W., "Flow over an All-Body Hypersonic Aircraft: Experiment and Computation," *Journal of Spacecraft and Rockets*, Vol. 29, No. 1, Jan.–Feb. 1992, pp. 7–15. doi:10.2514/3.26308

[28] Reda, D. C., Wilder, M. C., Bogdanoff, D. W., and Prabhu, D. K., "Transition Experiments on Blunt Bodies with Distributed Roughness in Hypersonic Free Flight," *Journal of Spacecraft and Rockets*, Vol. 45, No. 2, March–April 2008, pp. 210–215. doi:10.2514/1.30288

[29] Back, L. H., and Cuffel, R. F., "Changes in Heat Transfer from Turbulent Boundary Layers Interacting with Shock Waves and Expansion Waves," *AIAA Journal*, Vol. 8, No. 10, 1970, pp. 1871–1873. doi:10.2514/3.6004

[30] Holden, M. S., "Shock Wave-Turbulent Boundary Layer Interaction in High Speed Flow," ARL TR 75-0204, June 1975.

[31] AIAA, "Guide for the Verification and Validation of Computational Fluid Dynamics Simulations," AIAA Paper AIAA-G-077-1998(2002), Reston, VA, 6 May 1998.

[32] Coleman, H. W., and Stern, F., "Uncertainties and CFD Code Validation," *Journal of Fluids Engineering*, Vol. 119, Dec. 1997, pp. 795–802. doi:10.1115/1.2819500

[33] Roache, P. J., "Error Bars for CFD," AIAA Paper 2003-408, Jan. 2003.

[34] Oberkampf, W. L., and Trucano, T. G., "Verification and Validation in Computational Fluid Dynamics," AIAA Paper 2000-2549, June 2000.

[35] Oberkampf, W. L., and Barone, M. F., "Measures of Agreement Between Computation and Experiment: Validation Metrics," *Journal of Computational Physics*, Vol. 217, No. 1, 2006, pp. 5–36. doi:10.1016/j.jcp.2006.03.037

[36] Oberkampf, W. L., and Roy, C. J., *Verification and Validation in Scientific Computing*, Cambridge Univ. Press, Cambridge, England, U.K., 2010.

[37] Roy, C. J., and Oberkampf, W. L., "A Comprehensive Framework for Verification, Validation, and Uncertainty Quantification in Scientific Computing," *Computer Methods in Applied Mechanics and Engineering*, Vol. 200, 2011, pp. 2131–2144. doi:10.1016/j.cma.2011.03.016

[38] W. H. Beyer (ed.), *Handbook of Tables for Probability and Statistics*, 2nd ed., CRC, Cleveland, OH, 1968.

[39] Hill, T., and Lewicki, P., *Statistics Methods and Applications*, StatSoft, Tulsa, OK, 2007.

[40] Wright, M. J., White, T., and Mangini, N., "Data Parallel Line Relaxation Code User Manual, Acadia-Version 4.01.1," NASA TM-2009-215388, Oct. 2009.

[41] Baldwin, B., and Lomax, H., "Thin Layer Approximation and Algebraic Model for Separated Turbulent Flows," AIAA Paper 1978-257, 1978.

[42] Settles, G. S., and Dodson, L. J., "Hypersonic Shock/Boundary-Layer Interaction Database," NASA CR 177577, April 1991.

[43] Settles, G. S., and Dodson, L. J., "Supersonic and Hypersonic Shock/Boundary-Layer Interaction Database," *AIAA Journal*, Vol. 32, No. 7, July 1994, pp. 1377–1383. doi:10.2514/3.12205

[44] Roy, C. J., and Blottner, F. G., "Review and Assessment of Turbulence Models for Hypersonic Flows," AIAA Paper 2006-713, 2006.

[45] Knight, D., Yan, H. Y., Panaras, A. G., and Zheltovodov, A., "Advances in CFD Prediction of Shock Wave Turbulent Boundary Layer Interactions," *Progress in Aerospace Sciences*, Vol. 39, No. 2, 2003, pp. 121–184. doi:10.1016/S0376-0421(02)00069-6; also NATO Working Group 10, Rept. RTO-TR-AVT-007-V3.

[46] Bradshaw, P., "Bibliography Of Turbulent Flows, 1980-2002," http://navier.stanford.edu/bradshaw/pbref/intro.html [retrieved 3 July 2012].

[47] Schulein, E., Krogmann, P., and Stanewsky, E., "Documentation of Two-Dimensional Impinging Shock/Turbulent Boundary Layer Interaction Flow," DLR, German Aerospace Center, Rept. IB 223-96

A 49, Göttingen, Germany, Oct. 1996.
[48] Schulein, E., "Skin-Friction and Heat Flux Measurements in Shock/Boundary-Layer Interaction Flows," *AIAA Journal*, Vol. 44, No. 8, Aug. 2006, pp. 1732–1741. doi:10.2514/1.15110; also AIAA Paper 2004-2115, 2004.
[49] Tanner, L., and Blows, L., "A Study of the Motion of Oil Films on Surfaces in Air Flow, with Application to the Measurement of Skin Friction," *Journal of Physics E: Scientific Instruments*, Vol. 9, No. 3, 1976, pp. 194–202. doi:10.1088/0022-3735/9/3/015
[50] Monson, D., "Dual-Beam Skin Friction Interferometer," U.S. Patent 4377343, 22 March 1983.
[51] Brown, J. L., and Naughton, J. W., "The Thin Oil-Film Equation," NASA TM-1999-208767, March 1999.
[52] Brown, J. L., and Naughton, J. W., "Surface Imaging Skin Friction Instrument and Method," U.S. Patent 5,963,310, 5 Oct. 1999.
[53] Naughton, J. W., and Sheplak, M., "Modern Developments in Shear Stress Measurement," *Progress in Aerospace Sciences*, Vol. 38, Nos. 6–7, 2002, pp. 515–570. doi:10.1016/S0376-0421(02)00031-3
[54] Fedorova, N. N., Fedorchenko, I. A., and Schülein, E., "Experimental and Numerical Study of Oblique Shock Wave/Turbulent Boundary Layer Interaction at $M = 5$," *Computational Fluid Dynamics Journal*, Vol. 10, No. 3, Special Issue, Oct. 2001, pp. 390–395.
[55] Steelant, J., "Effect of a Compressibility Correction on Different Turbulence Models," *Engineering Turbulence Modelling and Experiments 5*, edited by W. Rodi and N. Fueyo, Elsevier, New York, 2002, pp. 207–216.
[56] Murray, N., "Three-Dimensional Turbulent Shock-Wave/Boundary-Layer Interactions in Hypersonic Flows," Ph.D. Dissertation, Imperial College, Univ. of London, London, 2007.
[57] Murray, N., and Hillier, R., "Separated Shock Wave/Turbulent Boundary Layer Interactions at Hypersonic Speeds," AIAA Paper 2006-3038, June 2006.
[58] Elfstrom, G. M., "Turbulent Hypersonic Flow at a Wedge-Compression Corner," *Journal of Fluid Mechanics*, Vol. 53, Part 1, 1972, pp. 113–127. doi:10.1017/S0022112072000060
[59] Coleman, G. T., and Stollery, J. L., "Heat Transfer from Hypersonic Turbulent Flow at a Wedge Compression Corner," *Journal of Fluid Mechanics*, Vol. 56, Part 4, 1972, pp. 741–752. doi:10.1017/S0022112072002630
[60] Boyce, R. R., and Hillier, R., "Shock-Induced Three-Dimensional Separation of an Axisymmetric Hypersonic Turbulent Boundary Layer," AIAA Paper 2000-2226, June 2000.
[61] Franz, J., http://www.frantz.fi/software/g3data.php [retrieved 3 July 2012].
[62] Mallinson, S. G., Gai, S. L., and Mudford, N. R., "Laminar Flows of High Enthalpy Air in a Compression Corner," 11th Australian Fluid Mechanics Conference, Univ. of Tasmania, Hobart, Australia, 14–18 Dec. 1992.
[63] Kussoy, M. I., and Horstman, K. C., "Documentation of Two- and Three-Dimensional Shock-Wave/Turbulent Boundary-Layer Interaction Flows at Mach 8.2," NASA TM 103838, May 1991.
[64] Kussoy, M. I., and Horstman, C. C., "Documentation of Two- and Three-Dimensional Hypersonic Shock-Wave/Turbulent Boundary-Layer Interaction Flows," NASA TM 101075, Jan. 1989.
[65] Park, C., *Nonequilibrium Hypersonic Aerothermodynamics*, Wiley, New York, 1990.
[66] Mallinson, S. G., Hillier, R., Jackson, A. P., Kirk, D. C., Soltani, S., and Zanchetta, M., "Gun Tunnel Flow Calibration: Defining Input Condition for Hypersonic Flow Computations," *Shock Waves*, Vol. 10, No. 5, 2000, pp. 313–322. doi:10.1007/s001930000064
[67] Vuong, S. T., and Coakley, T. J., "Modeling of Turbulence for Hypersonic Flows with and Without Separation," AIAA Paper 1987-0286, Reno, NV, Jan. 1987.
[68] Cebeci, T., and Smith, A. M. O., *Analysis of Turbulent Boundary Layers*, Vol. 15, Series in Applied Mathematics and Mechanics, Academic Press, Orlando, FL, 1974.
[69] Kato, M., and Launder, B. E., "The Modeling of Turbulent Flow Around Stationary and Vibrating Square Cylinders," *Proceedings of the 9th Symposium on Turbulent Shear Flows*, Kyoto, Aug. 1993, pp. 10.4.1–10.4.6.

D. Bose
Guest Editor